Kramers degeneracy in a magnetic field and Zeeman spin-orbit coupling in antiferromagnetic conductors

Revaz Ramazashvili*
ENS, LPTMS, UMR8626, Bât. 100, Université Paris-Sud, 91405 Orsay, France
(Received 9 May 2008; revised manuscript received 14 March 2009; published 29 May 2009)

In this paper, I analyze the symmetries and degeneracies of electron eigenstates in a commensurate collinear antiferromagnet. In a magnetic field transverse to the staggered magnetization, a hidden antiunitary symmetry protects double degeneracy of the Bloch eigenstates at a special set of momenta. In addition to this "Kramers degeneracy" subset, the manifold of momenta, labeling the doubly degenerate Bloch states in the Brillouin zone, may also contain an "accidental degeneracy" subset that is not protected by symmetry and that may change shape under perturbation. These degeneracies give rise to a substantial momentum dependence of the transverse g-factor in the Zeeman coupling, turning the latter into a spin-orbit interaction. I discuss a number of materials, where Zeeman spin-orbit coupling is likely to be present, and outline the simplest properties and experimental consequences of this interaction, that may be relevant to systems from chromium to borocarbides, cuprates, hexaborides, iron pnictides, as well as organic and heavy fermion conductors.

DOI: 10.1103/PhysRevB.79.184432 PACS number(s): 75.50.Ee

I. INTRODUCTION

Antiferromagnetism is widespread in materials with interesting electron properties. Chromium[1] and its alloys,[2,3] numerous borocarbides,[4] electron- and hole-doped cuprates,[5,6] iron pnictides,[7] and various organic[8] and heavy fermion[9–11] compounds all have an antiferromagnetic state present in their phase diagram. The physics of these antiferromagnetic phases has been a subject of active research.

In this paper, I study the response of electron Bloch eigenstates in an antiferromagnet to a weak magnetic field. I concentrate on the simplest case: a centrosymmetric doubly commensurate collinear antiferromagnet, shown schematically in Fig. 1, where the magnetization density at any point in space is parallel or antiparallel to a single fixed direction $\mathbf{n}$ of the staggered magnetization and changes sign upon primitive translation of the underlying lattice.

Below, I show that, in a magnetic field transverse to the staggered magnetization, a hidden antiunitary symmetry protects the Kramers degeneracy of Bloch eigenstates at a special set of momenta. This degeneracy gives rise to a peculiar spin-orbit coupling, whose emergence and basic properties, along with the degeneracy itself, are the main results of this work.

In a paramagnet, the double degeneracy of the Bloch eigenstates is commonly attributed to symmetry under time reversal θ—and, indeed, perturbations that break time-reversal symmetry (such as ferromagnetism or a magnetic field) do tend to remove the degeneracy. Yet violation of θ alone does not preclude degeneracy: in a commensurate centrosymmetric Néel antiferromagnet, as in a paramagnet, all Bloch eigenstates enjoy a Kramers degeneracy[12] in spite of time-reversal symmetry being broken in the former, but not in the latter.

In an antiferromagnet, the staggered magnetization sets a special direction $\mathbf{n}$ in electron-spin space, making it anisotropic. A magnetic field along $\mathbf{n}$ removes the degeneracy of all Bloch eigenstates, as it does in a paramagnet. By contrast, in a transverse field, a hidden antiunitary symmetry protects the Kramers degeneracy of Bloch eigenstates at a special set of momenta.

Generally, in d dimensions, the manifold of momenta corresponding to doubly degenerate Bloch states in a transverse field is $(d-1)$ dimensional; within a subset of this manifold, the degeneracy is dictated by symmetry. This is in marked contrast with what happens in a paramagnet, where an arbitrary magnetic field lifts the degeneracy of *all* Bloch eigenstates. For brevity, in this paper I often refer to the manifold of momenta, labeling the degenerate Bloch states in the Brillouin zone, as to the "degeneracy manifold."

As a consequence of the Kramers degeneracy of the special Bloch states in a transverse field, the transverse component $g_\perp$ of the electron g-tensor vanishes for such states. Not being identically equal to zero, $g_\perp$ must, therefore, carry a substantial momentum dependence, and the Zeeman coupling $\mathcal{H}_{\mathrm{ZSO}}$ must take the form

$$\mathcal{H}_{\mathrm{ZSO}} = -\mu_B[g_\parallel(\mathbf{H}_\parallel \cdot \boldsymbol{\sigma}) + g_\perp(\mathbf{p})(\mathbf{H}_\perp \cdot \boldsymbol{\sigma})], \qquad (1)$$

where $\mathbf{H}_\parallel = (\mathbf{H}\cdot\mathbf{n})\mathbf{n}$ and $\mathbf{H}_\perp = \mathbf{H} - \mathbf{H}_\parallel$ are the longitudinal and transverse components of the magnetic field with respect to the unit vector $\mathbf{n}$ of the staggered magnetization, μ_B is the Bohr magneton, while $g_\parallel$ and $g_\perp(\mathbf{p})$ are the longitudinal and transverse components of the g-tensor.

This significant momentum dependence of $g_\perp(\mathbf{p})$ turns the common Zeeman coupling into a kind of spin-orbit interaction $\mathcal{H}_{\mathrm{ZSO}}$ (1), whose appearance and key properties are the focus of this work. Zeeman spin-orbit coupling may manifest itself spectacularly in a number of ways, which will be mentioned below and discussed in detail elsewhere.

The symmetry properties of wave functions in magnetic crystals have been studied by Dimmock and Wheeler,[13] who pointed out, among other things, that magnetism not only lifts degeneracies by obviously lowering the symmetry, but also may introduce new ones. This may happen at the magnetic Brillouin-zone (MBZ) boundary under the necessary condition that the magnetic unit cell be larger than the paramagnetic one.[13]

For a Néel antiferromagnet on a lattice of square symmetry, the response of the electron states to a magnetic field was studied in Ref. 14 using symmetry arguments and in Ref. 15

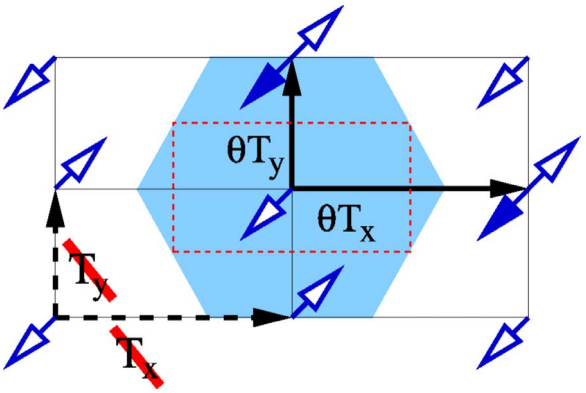

FIG. 1. (Color online) Doubly commensurate collinear antiferromagnet on a simple rectangular lattice. In the absence of magnetism, time reversal θ and primitive translations $\mathbf{T}_x$ and $\mathbf{T}_y$, shown by dashed arrows, are symmetry operations. In the antiferromagnetic state, neither of the three remains a symmetry, but the products $\theta\mathbf{T}_x$ and $\theta\mathbf{T}_y$, shown by solid arrows, do, as illustrated by filled spin arrows. Small dashed rectangle at the center is the Wigner-Seitz cell boundary in the paramagnetic state, while the shaded hexagon is its antiferromagnetic counterpart. Notice that neither of the point-group operations interchanges the two sublattices, hence any point symmetry of the lattice, including inversion $\mathcal{I}$, remains a symmetry of the antiferromagnetic state.

within a weak-coupling model. The present work is a detailed presentation of recent results.[16] It revisits Ref. 14, extends it to an arbitrary crystal symmetry and to a finite as opposed to infinitesimal magnetic field, and uncovers a rich interplay between the symmetry of magnetic structure and that of the underlying crystal lattice. At the same time, the present work extends Ref. 13 by allowing for an external magnetic field—to show how, at special momenta, the Kramers degeneracy in an antiferromagnet may persist even in a transverse magnetic field.

This work treats antiferromagnetic order as static, neglecting both its classical and quantum fluctuations. This excludes from consideration strongly fluctuating antiferromagnetic states such as those near a continuous phase transition, be it a finite-temperature Néel transition or a quantum ($T=0$) critical point. At the same time, the single-electron Bloch eigenstates, considered hereafter, must be well-defined. As in a normal Fermi-liquid state, this does not rule out strong interaction between electrons, but simply requires temperatures well below the Fermi energy. Finally, to justify the neglect of quantum fluctuations, the ordered magnetic moment must be of the order of or greater than the Bohr magneton.

As a consequence, the present theory applies to antiferromagnets (i) deep inside a commensurate long-range antiferromagnetic state and far enough from any continuous Néel transition, finite-temperature or quantum, (ii) with an ordered moment noticeable on the scale of the Bohr magneton, and (iii) far below both the Néel and the effective Fermi temperatures. All materials mentioned in Sect. IV are meant to be considered under these conditions.

The paper is organized as follows. Section II opens with a reminder of how, in spite of broken time-reversal symmetry, all Bloch eigenstates in a commensurate collinear antiferromagnet retain Kramers degeneracy, provided there is an inversion center.[12] Then I show how, even in a transverse magnetic field, a hidden symmetry of antiferromagnetic order may protect the Kramers degeneracy for certain Bloch states. Section III establishes several properties of the single-electron spectrum in a weakly coupled antiferromagnet, subject to a transverse magnetic field.

Section IV contains the analysis of simple examples that may be relevant to specific materials from chromium to organic conductors, from borocarbides to underdoped cuprates, and to various heavy fermion metals. Section V reviews the findings and examines them in the light of earlier work, while the Appendices A–D present various technical details.

II. GENERAL ARGUMENTS

It is convenient to begin by describing the crystal host symmetry in the absence of magnetism, with the average magnetization density notionally set to zero.[13] I refer to this as to the paramagnetic state symmetry, even though the symmetry of the actual paramagnetic state may be different, for instance, due to a lattice distortion upon transition. Unitary symmetries of the paramagnetic state form a group, h, which includes a set of elementary translations $\mathbf{T}_\mathbf{a}$ by primitive translation vectors $\mathbf{a}$. Time reversal θ being indeed a symmetry of the paramagnetic state, the full symmetry group g of the paramagnetic state includes h, and products of θ with each element of h: $g=h+\theta h$; put otherwise, h is an invariant unitary subgroup of g.

Antiferromagnetic order couples to the electron spin $\boldsymbol{\sigma}$ via the exchange term $(\boldsymbol{\Delta}_\mathbf{r}\cdot\boldsymbol{\sigma})$, where $\boldsymbol{\Delta}_\mathbf{r}$ is proportional to the average microscopic magnetization at point $\mathbf{r}$. In keeping with the arguments of Sec. I, fluctuations of $\boldsymbol{\Delta}_\mathbf{r}$ are neglected. Being of relativistic origin, spin-orbit couplings of the crystal lattice to the electron spin and to the magnetization density are also neglected. This is a good approximation in a broad range of problems, at the very least at temperatures above the scale set by the spin-orbit coupling (see Sec. V for details). In this "exchange symmetry" approximation,[17] magnetization density and electron spin are assigned to a separate space, independent of the real space of the crystal; this makes coordinate rotations and other point symmetries inert with respect to $\boldsymbol{\Delta}_\mathbf{r}$ and $\boldsymbol{\sigma}$.

A nonzero $\boldsymbol{\Delta}_\mathbf{r}$ changes sign under time reversal θ and removes the symmetry under primitive translations $\mathbf{T}_\mathbf{a}$, thus reducing the symmetry with respect to that of paramagnetic state. In a doubly commensurate collinear antiferromagnet, $\boldsymbol{\Delta}_\mathbf{r}$ changes sign upon $\mathbf{T}_\mathbf{a}$: $\boldsymbol{\Delta}_{\mathbf{r}+\mathbf{a}}=-\boldsymbol{\Delta}_\mathbf{r}$, while $\mathbf{T}_\mathbf{a}^2$ leaves $\boldsymbol{\Delta}_\mathbf{r}$ intact: $\boldsymbol{\Delta}_{\mathbf{r}+2\mathbf{a}}=\boldsymbol{\Delta}_\mathbf{r}$. Even though neither θ nor $\mathbf{T}_\mathbf{a}$ remains a symmetry, their product $\theta\mathbf{T}_\mathbf{a}$ does (see Fig. 1). In a centrosymmetric system, so does $\theta\mathbf{T}_\mathbf{a}\mathcal{I}$, where $\mathcal{I}$ is inversion. The importance of the combined symmetry $\theta\mathbf{T}_\mathbf{a}\mathcal{I}$ will become clear in Sec. II A.

Together with the uniaxial character ($\boldsymbol{\Delta}_\mathbf{r}$ at any point $\mathbf{r}$ pointing along or against the single direction $\mathbf{n}$ of staggered magnetization), these relations define a commensurate collinear Néel antiferromagnet via transformation properties of its microscopic magnetization density.

A. Kramers degeneracy in zero field

The combined antiunitary symmetry $\theta \mathbf{T}_\mathbf{a}\mathcal{I}$ gives rise to a Kramers degeneracy.[12] If $|\mathbf{p}\rangle$ is a Bloch eigenstate at momentum $\mathbf{p}$, then $\theta \mathbf{T}_\mathbf{a}\mathcal{I}|\mathbf{p}\rangle$ is degenerate with $|\mathbf{p}\rangle$. Since θ and $\mathcal{I}$ both invert the momentum, both $|\mathbf{p}\rangle$ and $\theta \mathbf{T}_\mathbf{a}\mathcal{I}|\mathbf{p}\rangle$ carry the same momentum label $\mathbf{p}$. Formally, this is verified by the action of any translation $\mathbf{T}_\mathbf{b}$ that remains a symmetry of the antiferromagnetic state

$$\mathbf{T}_\mathbf{b}\theta \mathbf{T}_\mathbf{a}\mathcal{I}|\mathbf{p}\rangle = \theta \mathbf{T}_\mathbf{a}\mathbf{T}_\mathbf{b}\mathcal{I}|\mathbf{p}\rangle = \theta \mathbf{T}_\mathbf{a}\mathcal{I}\mathbf{T}_{-\mathbf{b}}|\mathbf{p}\rangle = \theta \mathbf{T}_\mathbf{a}\mathcal{I}e^{-i\mathbf{p}\cdot\mathbf{b}}|\mathbf{p}\rangle = e^{i\mathbf{p}\cdot\mathbf{b}}\theta \mathbf{T}_\mathbf{a}\mathcal{I}|\mathbf{p}\rangle. \quad (2)$$

At the same time, $|\mathbf{p}\rangle$ and $\theta \mathbf{T}_\mathbf{a}\mathcal{I}|\mathbf{p}\rangle$ are orthogonal. This follows from Eq. (A2) as soon as one chooses $\mathcal{O}=\mathbf{T}_\mathbf{a}\mathcal{I}$ and $|\psi\rangle=|\mathbf{p}\rangle$. As a consequence of the electron carrying spin-$\frac{1}{2}$, $\theta^2=-1$. Recalling that $(\mathbf{T}_\mathbf{a}\mathcal{I})^2=1$ and hence $(\theta \mathbf{T}_\mathbf{a}\mathcal{I})^2=-1$, one finds

$$\langle \mathbf{p}|\mathcal{I}\mathbf{T}_\mathbf{a}\theta|\mathbf{p}\rangle = -\langle \mathbf{p}|\mathcal{I}\mathbf{T}_\mathbf{a}\theta|\mathbf{p}\rangle. \quad (3)$$

Thus, in spite of broken time-reversal symmetry, in a centrosymmetric commensurate Néel antiferromagnet *all* Bloch states retain a Kramers degeneracy.

B. Kramers degeneracy in a transverse field

Generally, a magnetic field $\mathbf{H}$ lifts this degeneracy. However, in a transverse field, a hidden antiunitary symmetry may protect the degeneracy at a special set of points in the Brillouin zone, as I show below.

In an antiferromagnet, subject to a magnetic field $\mathbf{H}$, the single-electron Hamiltonian takes the form

$$\mathcal{H} = \mathcal{H}_0 + (\mathbf{\Delta}_\mathbf{r}\cdot\boldsymbol{\sigma}) - (\mathbf{H}\cdot\boldsymbol{\sigma}), \quad (4)$$

where the "paramagnetic" part $\mathcal{H}_0$ is invariant under independent action of $\mathbf{T}_\mathbf{a}$ and θ, and where $g\mu_B$ is set to unity. In the absence of the field, all Bloch eigenstates of the Hamiltonian (4) are doubly degenerate by virtue of Eq. (3).

Consider the symmetries of the Hamiltonian (4), involving a combination of an elementary translation $\mathbf{T}_\mathbf{a}$, time reversal θ, or a spin rotation $\mathbf{U}_\mathbf{m}(\phi)$ around an axis $\mathbf{m}$ by an angle ϕ. These symmetries are listed in Table I; the relative orientation of $\mathbf{\Delta}_\mathbf{r}$, $\mathbf{H}_\parallel$, and $\mathbf{H}_\perp$ is shown in Fig. 2. The transverse field $\mathbf{H}_\perp$ breaks the symmetries $\mathbf{U}_\mathbf{n}(\phi)$ and $\mathbf{T}_\mathbf{a}\theta$, but preserves their combination at $\phi=\pi$, i.e., $\mathbf{U}_\mathbf{n}(\pi)\mathbf{T}_\mathbf{a}\theta$. Acting on an exact Bloch state $|\mathbf{p}\rangle$ at momentum $\mathbf{p}$, this combined antiunitary operator creates a degenerate partner eigenstate $\mathbf{U}_\mathbf{n}(\pi)\mathbf{T}_\mathbf{a}\theta|\mathbf{p}\rangle$, which is orthogonal to $|\mathbf{p}\rangle$ everywhere in the Brillouin zone unless $(\mathbf{p}\cdot\mathbf{a})$ is an integer multiple of π (in other words, unless $\mathbf{p}$ lies at a paramagnetic Brillouin-zone boundary)

$$\langle \mathbf{p}|\mathbf{U}_\mathbf{n}(\pi)\mathbf{T}_\mathbf{a}\theta|\mathbf{p}\rangle = e^{-2i(\mathbf{p}\cdot\mathbf{a})}\langle \mathbf{p}|\mathbf{U}_\mathbf{n}(\pi)\mathbf{T}_\mathbf{a}\theta|\mathbf{p}\rangle. \quad (5)$$

Equation (5) follows from Eq. (A2) for $\mathcal{O}=\mathbf{U}_\mathbf{n}(\pi)\mathbf{T}_\mathbf{a}$ and $|\psi\rangle=|\mathbf{p}\rangle$ as soon as one observes that $[\mathbf{U}_\mathbf{n}(\pi)\mathbf{T}_\mathbf{a}\theta]^2=\mathbf{T}_\mathbf{a}^2=\mathbf{T}_{2\mathbf{a}}$. In a magnetic field, double translation $\mathbf{T}_{2\mathbf{a}}$ remains a symmetry; according to the Bloch theorem, it acts on $|\mathbf{p}\rangle$ as per $\mathbf{T}_{2\mathbf{a}}|\mathbf{p}\rangle=e^{2i(\mathbf{p}\cdot\mathbf{a})}|\mathbf{p}\rangle$, thus leading to Eq. (5).

Notice, however, that the eigenstate $\mathbf{U}_\mathbf{n}(\pi)\mathbf{T}_\mathbf{a}\theta|\mathbf{p}\rangle$ carries momentum label $-\mathbf{p}$ rather than $\mathbf{p}$. By contrast with the case of zero field, combining $\mathbf{U}_\mathbf{n}(\pi)\mathbf{T}_\mathbf{a}\theta$ with inversion $\mathcal{I}$ no longer helps to produce a degenerate partner eigenstate at the original momentum $\mathbf{p}$: since θ, $\mathbf{U}_\mathbf{n}(\pi)$, and $\mathbf{T}_\mathbf{a}\mathcal{I}$ all commute and since $[\mathcal{I}\mathbf{U}_\mathbf{n}(\pi)\mathbf{T}_\mathbf{a}\theta]^2=1$, Eq. (A2) for $\mathcal{O}=\mathcal{I}\mathbf{U}_\mathbf{n}(\pi)\mathbf{T}_\mathbf{a}$ and $|\psi\rangle=|\mathbf{p}\rangle$ only confirms that $\langle \mathbf{p}|\mathcal{I}\mathbf{U}_\mathbf{n}(\pi)\mathbf{T}_\mathbf{a}\theta|\mathbf{p}\rangle$ equals itself.

TABLE I. Symmetries of a collinear doubly commensurate antiferromagnet. The left column is for zero field, central column for a transverse magnetic field $\mathbf{H}_\perp$, and the right column for a longitudinal field $\mathbf{H}_\parallel$. As above, $\mathbf{T}_\mathbf{a}$ denotes an elementary translation by $\mathbf{a}$. As shown in Fig. 2, the unit vector $\mathbf{n}$ is collinear with $\mathbf{\Delta}_\mathbf{r}$, the unit vector $\mathbf{h}$ points along $\mathbf{H}_\perp$, and the unit vector $\mathbf{l}$ is defined via $\mathbf{l}=\mathbf{n}\times\mathbf{h}$. For a general orientation of the field ($\mathbf{H}_\parallel\neq 0$, $\mathbf{H}_\perp\neq 0$), not shown in this table, $\mathbf{U}_\mathbf{l}(\pi)\theta$ is the only surviving symmetry, where $\mathbf{U}_\mathbf{m}(\phi)$ denotes spin rotation by angle ϕ around the $\mathbf{m}$ axis.

$(\mathbf{\Delta}_\mathbf{r}\cdot\boldsymbol{\sigma})$	$(\mathbf{\Delta}_\mathbf{r}\cdot\boldsymbol{\sigma})+(\mathbf{H}_\perp\cdot\boldsymbol{\sigma})$	$(\mathbf{\Delta}_\mathbf{r}\cdot\boldsymbol{\sigma})+(\mathbf{H}_\parallel\cdot\boldsymbol{\sigma})$
$\mathbf{U}_\mathbf{n}(\phi)$		$\mathbf{U}_\mathbf{n}(\phi)$
$\mathbf{U}_\mathbf{h}(\pi)\mathbf{T}_\mathbf{a}$	$\mathbf{U}_\mathbf{h}(\pi)\mathbf{T}_\mathbf{a}$	
$\mathbf{U}_\mathbf{l}(\pi)\mathbf{T}_\mathbf{a}$		
$\mathbf{T}_\mathbf{a}\theta$	$\mathbf{U}_\mathbf{n}(\pi)\mathbf{T}_\mathbf{a}\theta$	
$\mathbf{U}_\mathbf{h}(\pi)\theta$		$\mathbf{U}_\mathbf{h}(\pi)\theta$
$\mathbf{U}_\mathbf{l}(\pi)\theta$	$\mathbf{U}_\mathbf{l}(\pi)\theta$	$\mathbf{U}_\mathbf{l}(\pi)\theta$

Thus, for an exact Bloch state $|\mathbf{p}\rangle$ at momentum $\mathbf{p}$, the antiunitary symmetry $\mathbf{U}_\mathbf{n}(\pi)\mathbf{T}_\mathbf{a}\theta$ produces an orthogonal degenerate eigenstate $\mathbf{U}_\mathbf{n}(\pi)\mathbf{T}_\mathbf{a}\theta|\mathbf{p}\rangle$ at momentum $-\mathbf{p}$. The two momenta $\mathbf{p}$ and $-\mathbf{p}$ are different, with one key exception. It occurs for $\mathbf{p}$ at the magnetic Brillouin zone boundary, given a unitary symmetry $\mathcal{U}$, that transforms $-\mathbf{p}$ into a momentum, equivalent to $\mathbf{p}$ up to a reciprocal-lattice vector $\mathbf{Q}$ of the antiferromagnetic state[13]

$$-\mathcal{U}\mathbf{p} = \mathbf{p} + \mathbf{Q}. \quad (6)$$

In this case, the eigenstate $\mathcal{U}\mathbf{U}_\mathbf{n}(\pi)\mathbf{T}_\mathbf{a}\theta|\mathbf{p}\rangle$ carries momentum label $\mathbf{p}+\mathbf{Q}\equiv\mathbf{p}$; this eigenstate is degenerate with $|\mathbf{p}\rangle$ and orthogonal to it, thus explicitly demonstrating the Kramers

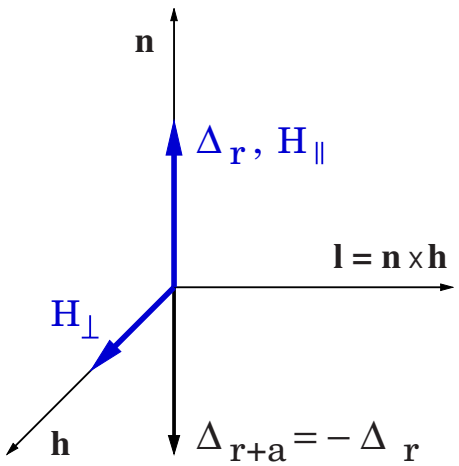

FIG. 2. (Color online) Relative orientation of $\mathbf{\Delta}_\mathbf{r}$, $\mathbf{\Delta}_{\mathbf{r}+\mathbf{a}}$, $\mathbf{H}_\parallel$, and $\mathbf{H}_\perp$. To see the combined symmetries of Table I, notice that θ flips both $\mathbf{\Delta}_\mathbf{r}$ and $\mathbf{H}$, while $\mathbf{T}_\mathbf{a}$ leaves $\mathbf{H}$ intact, but inverts $\mathbf{\Delta}_\mathbf{r}$. Unit vectors $\mathbf{n}$, $\mathbf{h}$, and $\mathbf{l}=\mathbf{n}\times\mathbf{h}$ are defined as shown.

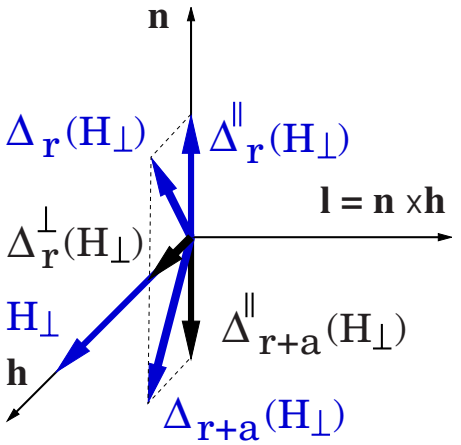

FIG. 3. (Color online) Relative orientation of $\boldsymbol{\Delta}_{\mathbf{r}}(H_\perp)$ and $\boldsymbol{\Delta}_{\mathbf{r+a}}(H_\perp)$, tilted by a transverse field $\mathbf{H}_\perp$. The component $\boldsymbol{\Delta}^{\perp}_{\mathbf{r}}(H_\perp)$ along the field is periodic under elementary translation $\mathbf{T_a}$: $\boldsymbol{\Delta}^{\perp}_{\mathbf{r+a}}(H_\perp)=\boldsymbol{\Delta}^{\perp}_{\mathbf{r}}(H_\perp)$; the component along the zero field $\boldsymbol{\Delta}_{\mathbf{r}}$ is antiperiodic: $\boldsymbol{\Delta}^{\parallel}_{\mathbf{r+a}}(H_\perp)=-\boldsymbol{\Delta}^{\parallel}_{\mathbf{r}}(H_\perp)$.

degeneracy at momentum $\mathbf{p}$ in a transverse field. This result is general: combined with any momentum-inverting antiunitary symmetry, Eq. (6) leads to a Kramers degeneracy at momentum $\mathbf{p}$.[13] The simplest illustration, where $\mathcal{U}$ is the unity operator, is given by $\mathbf{p}=\mathbf{Q}/2$ and shown in Figs. 5 and 6(a) for two particular cases. These and other examples are described in Sec. IV. Notice that, at $\mathbf{p}=\mathbf{Q}/2$ (with $\mathcal{U}=1$), the degeneracy in a transverse field is guaranteed even for a low crystal symmetry, provided an inversion center. Also notice, once more, that $\mathcal{U}$, $\mathcal{I}$, and other point symmetries above are inert with respect to spin as a consequence of the exchange symmetry approximation.[17]

The Hamiltonian (4) and the subsequent analysis ignored the response of the antiferromagnetic order to the transverse field $\mathbf{H}_\perp$. This, however, does not affect the set of points, where the Kramers degeneracy in a transverse field is protected by the antiunitary symmetry $\mathcal{U}\mathbf{U_n}(\pi)\mathbf{T_a}\theta$. Upon application of $\mathbf{H}_\perp$, the Néel sublattices tilt toward the field, making it convenient to present $\boldsymbol{\Delta}_{\mathbf{r}}$ as

$$\boldsymbol{\Delta}_{\mathbf{r}}(H_\perp)=\boldsymbol{\Delta}^{\perp}_{\mathbf{r}}(H_\perp)+\boldsymbol{\Delta}^{\parallel}_{\mathbf{r}}(H_\perp), \tag{7}$$

where $\boldsymbol{\Delta}^{\perp}_{\mathbf{r}}(H_\perp)$ points along $\mathbf{H}_\perp$ and $\boldsymbol{\Delta}^{\parallel}_{\mathbf{r}}(H_\perp)$ points along $\mathbf{n}$, as shown in Fig. 3. Since $\boldsymbol{\Delta}^{\perp}_{\mathbf{r+a}}(H_\perp)=\boldsymbol{\Delta}^{\perp}_{\mathbf{r}}(H_\perp)$ and $\boldsymbol{\Delta}^{\parallel}_{\mathbf{r+a}}(H_\perp)=-\boldsymbol{\Delta}^{\parallel}_{\mathbf{r}}(H_\perp)$, the second column of Table I remains intact upon replacing $\boldsymbol{\Delta}_{\mathbf{r}}$ in Hamiltonian (4) by $\boldsymbol{\Delta}_{\mathbf{r}}(H_\perp)$ of Eq. (7).

If the antiferromagnetic unit cell is a multiple of its paramagnetic counterpart, the magnetic Brillouin-zone boundary contains a set of points that do not belong to the paramagnetic Brillouin zone boundary (for example, see Figs. 5 and 6). In the paramagnetic state, no two points of this set, separated by antiferromagnetic reciprocal-lattice vector $\mathbf{Q}$ and satisfying condition (6), can be declared equivalent. As a curious consequence, the magnetic group of such a wave vector is *not* a subgroup of its paramagnetic counterpart.[13] Hence the degeneracy, if present, does hinge on magnetic order.

III. CLUES FROM WEAK COUPLING

Additional insight into the locus of states, that remain degenerate in a transverse magnetic field, is afforded by a weak-coupling single-electron Hamiltonian in a doubly commensurate collinear antiferromagnet. Let $\mathbf{Q}$ be the antiferromagnetic ordering wave vector (see the examples below); $\boldsymbol{\Delta}_{\mathbf{r}}$ creates a matrix element $(\boldsymbol{\Delta}\cdot\boldsymbol{\sigma})$ between the Bloch states at momenta $\mathbf{p}$ and $\mathbf{p}+\mathbf{Q}$ (for simplicity, I neglect its possible dependence on $\mathbf{p}$). Sublattice canting in a transverse field is taken into account in Appendix B. In magnetic field $\mathbf{H}$ and at weak coupling, Hamiltonian (4) takes the form[15]

$$\mathcal{H}=\begin{bmatrix}\epsilon_{\mathbf{p}}-(\mathbf{H}\cdot\boldsymbol{\sigma}) & (\boldsymbol{\Delta}\cdot\boldsymbol{\sigma})\\ (\boldsymbol{\Delta}\cdot\boldsymbol{\sigma}) & \epsilon_{\mathbf{p+Q}}-(\mathbf{H}\cdot\boldsymbol{\sigma})\end{bmatrix}, \tag{8}$$

where $\epsilon_{\mathbf{p}}$ and $\epsilon_{\mathbf{p+Q}}$ are single-particle energies of $\mathcal{H}_0$ in Eq. (4) at momenta $\mathbf{p}$ and $\mathbf{p}+\mathbf{Q}$, and the "bare" g-tensor in $(\mathbf{H}\cdot\boldsymbol{\sigma})$ is omitted for brevity.

In a purely transverse field $\mathbf{H}_\perp$, this Hamiltonian can be diagonalized simply by choosing the $\hat{z}$ axis in spin space along $\mathbf{H}_\perp$ and the $\hat{x}$ axis along $\boldsymbol{\Delta}$. As a result, the Hamiltonian (8) splits into two decoupled pieces: $\mathcal{H}_1(\mathbf{p},\mathbf{H}_\perp)$ for the amplitudes $|\mathbf{p};\uparrow\rangle$ and $|\mathbf{p}+\mathbf{Q};\downarrow\rangle$ and $\mathcal{H}_2(\mathbf{p},\mathbf{H}_\perp)$ for the amplitudes $|\mathbf{p};\downarrow\rangle$ and $|\mathbf{p}+\mathbf{Q};\uparrow\rangle$,

$$\mathcal{H}_{1(2)}(\mathbf{p},\mathbf{H}_\perp)=\begin{bmatrix}\epsilon_{\mathbf{p}}\mp H_\perp & \Delta\\ \Delta & \epsilon_{\mathbf{p+Q}}\pm H_\perp\end{bmatrix}. \tag{9}$$

The spectra $\mathcal{E}_{1(2)}(\mathbf{p})$ of $\mathcal{H}_{1(2)}$ are given by

$$\mathcal{E}_{1(2)}(\mathbf{p},\mathbf{H}_\perp)=\eta_{\mathbf{p}}\pm\sqrt{\Delta^2+[\zeta_{\mathbf{p}}\mp(\mathbf{H}_\perp\cdot\boldsymbol{\sigma})]^2}, \tag{10}$$

with the eigenvalue $H_\perp$ of $(\mathbf{H}_\perp\cdot\boldsymbol{\sigma})$ corresponding to $\mathcal{H}_1$, and the eigenvalue $-H_\perp$ to $\mathcal{H}_2$, and with $\eta_{\mathbf{p}}\equiv\frac{\epsilon_{\mathbf{p}}+\epsilon_{\mathbf{p+Q}}}{2}$ and $\zeta_{\mathbf{p}}\equiv\frac{\epsilon_{\mathbf{p}}-\epsilon_{\mathbf{p+Q}}}{2}$. The same spectrum can be obtained by excluding, say, $|\mathbf{p}+\mathbf{Q};\sigma\rangle$ from the eigenvalue equation for Eq. (8), but it is important to keep in mind that $\boldsymbol{\sigma}$ in Eq. (10) no longer describes spin, but rather pseudospin: since $(\mathbf{H}_\perp\cdot\boldsymbol{\sigma})$ does not commute with the Hamiltonian, the eigenstates of $\mathcal{H}_{1(2)}$ are superpositions of spin-up and spin-down states.

Equation (10) illustrates a number of points. First, the electron spectrum acquires a gap of size 2Δ. Second, in the absence of magnetic field, each eigenstate is indeed doubly degenerate, in agreement with the arguments, encapsulated in Eq. (3). Third, Eq. (10) shows, that the degeneracy persists in a transverse field [and, therefore, $g_\perp(\mathbf{p})$ in Eq. (1) vanishes] whenever $\zeta_{\mathbf{p}}=0$. Barring a special situation, this equation defines a surface in three dimensions, a line in two, and a set of points in one. This result for the dimensionality of the manifold of degenerate states hinges solely on the symmetry of the antiferromagnetic state and holds beyond weak coupling, as shown in Appendix C. Furthermore, as shown above, this manifold must contain all points, satisfying Eq. (6): the points, where the degeneracy is enforced by symmetry. Finally, expansion of Eq. (10) to first order in $(\mathbf{H}_\perp\cdot\boldsymbol{\sigma})$ yields the expression for $g_\perp(\mathbf{p})$ in Eq. (1) within the weak-coupling model (8)

$$g_\perp(\mathbf{p})=\frac{\zeta_{\mathbf{p}}}{\sqrt{\Delta^2+\zeta_{\mathbf{p}}^2}}. \tag{11}$$

At the end of Sec. II, I showed that tilting of the Néel sublattices in a transverse field does not affect the set of points, where the Kramers degeneracy in a transverse field is protected by the antiunitary symmetry $\mathcal{U}\mathbf{U_n}(\pi)\mathbf{T_a}\theta$. However, generally, the rest of the degeneracy manifold is not protected by symmetry and may change shape upon crystal deformation or under another perturbation. For instance, while leaving intact the symmetry-protected set of degeneracy points, the sublattice canting may change the shape of the unprotected part of the degeneracy manifold $g_\perp(\mathbf{p})=0$ compared to $\zeta_\mathbf{p}=0$. This effect is discussed in Appendix B.

Put otherwise, the degeneracy manifold may be divided into two parts. The first part is the "Kramers degeneracy" subset of special momenta, fixed by a conspiracy between the antiunitary symmetry $\mathbf{U_n}(\pi)\mathbf{T_a}\theta$ and the crystal symmetry. This "Kramers" subset is insensitive to perturbations that leave intact the crystal symmetry of the material. The rest is an "accidental" degeneracy subset, whose geometry, by contrast, may vary under perturbations, that do not affect the crystal symmetry, but only alter the microscopic parameters of the system. This division of the degeneracy manifold into a Kramers and an accidental degeneracy subsets is well illustrated by the examples of two-dimensional rectangular and square-symmetry antiferromagnets in Sec. IV.

A. Spectral symmetries in momentum space

The spectrum of the Hamiltonian (8) enjoys a number of symmetries. First, inversion symmetry makes the spectrum even under inversion. At the same time, $g_\perp(\mathbf{p})(\mathbf{H}_\perp\cdot\boldsymbol{\sigma})$ must also be even under inversion, which implies

$$g_\perp(-\mathbf{p})=g_\perp(\mathbf{p}). \tag{12}$$

The antiunitary symmetry $\mathbf{U_I}(\pi)\theta$ in the last line of Table I is another reason for $g_\perp(\mathbf{p})$ to be even under inversion, as $\mathbf{U_I}(\pi)\theta$ turns $g_\perp(\mathbf{p})(\mathbf{H}_\perp\cdot\boldsymbol{\sigma})$ into $g_\perp(-\mathbf{p})(\mathbf{H}_\perp\cdot\boldsymbol{\sigma})$.

Periodicity doubling due to antiferromagnetism manifests itself more interestingly. The ordering wave vector $\mathbf{Q}$ being a reciprocal lattice vector, any Bloch eigenstate at momentum $\mathbf{p}$ must have a degenerate partner eigenstate at momentum $\mathbf{p}+\mathbf{Q}$. Usually, this implies $\mathbf{Q}$-periodicity of any given band: $\epsilon(\mathbf{p})=\epsilon(\mathbf{p}+\mathbf{Q})$, which is the case, for instance, in a longitudinal field $\mathbf{H}_\parallel$, where $\mathcal{E}(\mathbf{p})$ undergoes the common Zeeman splitting $\mathcal{E}(\mathbf{p})\to\mathcal{E}(\mathbf{p})\pm H_\parallel$. In a Néel antiferromagnet in a transverse field, this is not the case: for a general $\mathbf{p}$, $\mathcal{E}_{1(2)}(\mathbf{p}+\mathbf{Q})\neq\mathcal{E}_{1(2)}(\mathbf{p})$. Instead,

$$\mathcal{E}_1(\mathbf{p}+\mathbf{Q},\mathbf{H}_\perp)=\mathcal{E}_2(\mathbf{p},\mathbf{H}_\perp), \tag{13}$$

while both $\mathcal{E}_1(\mathbf{p})$ and $\mathcal{E}_2(\mathbf{p})$ of Eq. (10) are invariant under momentum shift $\mathbf{p}\to\mathbf{p}+2\mathbf{Q}$. These properties are illustrated in Fig. 4, showing the splitting of a one-dimensional conduction band in a transverse field.

The reason behind Eq. (13) is that, as long as $H_\perp\neq 0$, neither $\mathcal{H}_1$ nor $\mathcal{H}_2$ in Eq. (9) is invariant under the momentum boost $\mathbf{p}\to\mathbf{p}+\mathbf{Q}$ in spite of the Hamiltonians (4) and (8) both having doubled periodicity. Rather,

$$\mathcal{H}_1(\mathbf{p}+\mathbf{Q},\mathbf{H}_\perp)=\mathcal{H}_2(\mathbf{p},\mathbf{H}_\perp), \tag{14}$$

which is made explicit by subsequent exchange of the diagonal matrix elements and leads to Eq. (13).

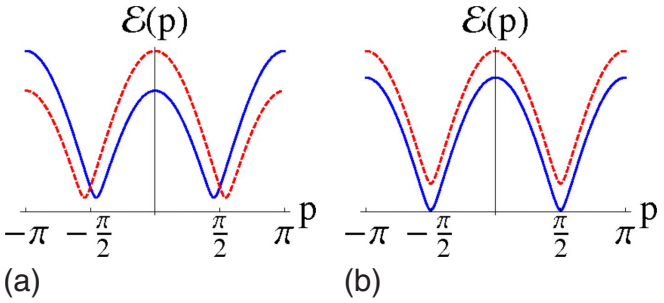

FIG. 4. (Color online) One-dimensional conduction-band splitting. (a) Conduction band ["+" sign in front of the square root in Eq. (10)], split by a transverse field. Here Eq. (13) is illustrated by the spectrum (10) for a nearest-neighbor hopping $\epsilon_\mathbf{p}=t\cos p$ in Hamiltonian (8). Notice that, in spite of the period doubling in real space, neither of the two split spectra has period π; instead, both are 2π-periodic, but map onto each other upon translation by π. Also notice that the two split subbands intersect at the symmetry-enforced degeneracy point $\mathbf{p}=\pm\frac{\pi}{2}$, as they should (see the one-dimensional example of Sec IV). (b) The conduction band, split by a longitudinal field. By contrast with (a), each split subband is π-periodic and degeneracy is lifted for all momenta.

Zeeman splitting corresponds to the difference $\mathcal{E}_1(\mathbf{p},\mathbf{H}_\perp)-\mathcal{E}_2(\mathbf{p},\mathbf{H}_\perp)$; hence it changes sign upon momentum shift by $\mathbf{Q}$. At the same time, direct inspection shows that Hamiltonians $\mathcal{H}_1$ and $\mathcal{H}_2$ in Eq. (9) turn into one another upon inversion of $\mathbf{H}_\perp$: $\mathcal{H}_1(\mathbf{p},-\mathbf{H}_\perp)=\mathcal{H}_2(\mathbf{p},\mathbf{H}_\perp)$. Combining this with Eq. (14), one finds that momentum boost by $\mathbf{Q}$ accompanied by inversion of $\mathbf{H}_\perp$ is a symmetry of both $\mathcal{H}_1$ and $\mathcal{H}_2$,

$$\mathcal{H}_{1(2)}(\mathbf{p}+\mathbf{Q},-\mathbf{H}_\perp)=\mathcal{H}_{1(2)}(\mathbf{p},\mathbf{H}_\perp). \tag{15}$$

For the transverse Zeeman term $g_\perp(\mathbf{p})(\mathbf{H}_\perp\cdot\boldsymbol{\sigma})$, this yields

$$g_\perp(\mathbf{p}+\mathbf{Q})=-g_\perp(\mathbf{p}). \tag{16}$$

Combined, Eqs. (12) and (16) lead to

$$g_\perp\left(\frac{\mathbf{Q}}{2}+\mathbf{p}\right)=-g_\perp\left(\frac{\mathbf{Q}}{2}-\mathbf{p}\right). \tag{17}$$

This implies not only that $g_\perp(\mathbf{p})$ must vanish at $\mathbf{p}=\frac{\mathbf{Q}}{2}$, but also that $g_\perp(\frac{\mathbf{Q}}{2}+\mathbf{p})$ is an odd function of $\mathbf{p}$. Taking into account the sublattice tilting does not modify any of the conclusions of this section (see Appendix B).

IV. EXAMPLES

In this section, I describe the manifolds of degenerate states for a number of concrete examples and thus show that the Zeeman spin-orbit coupling (1) is at work in many materials of great interest. It gives rise to various interesting phenomena, some of which are outlined in Sec. V C.

The Kramers degeneracy in a transverse field and the Zeeman spin-orbit coupling (1) will manifest themselves whenever carriers are present at or near the manifold of degenerate states $g_\perp(\mathbf{p})=0$. In a weakly doped antiferromagnetic insulator, this will happen whenever the relevant band extremum falls at or near the manifold of degenerate states. In an anti-

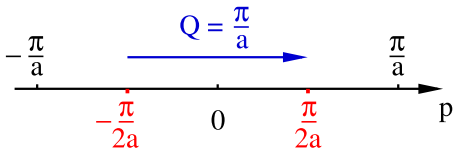

FIG. 5. (Color online) The paramagnetic ($\mathbf{p}=\pm\frac{\pi}{a}$) and the antiferromagnetic ($\mathbf{p}=\pm\frac{\pi}{2a}$) Brillouin zone boundaries of a one-dimensional Néel antiferromagnet. In the antiferromagnetic state, the two points $\mathbf{p}=\pm\frac{\pi}{2a}$ are identical up to the reciprocal-lattice vector $\mathbf{Q}=\frac{\pi}{a}$ of the antiferromagnetic state. At these two points, the antiunitary symmetry $\mathbf{U_n}(\pi)\mathbf{T_a}\theta$ protects the Kramers degeneracy against a transverse magnetic field.

ferromagnetic metal, this occurs when the Fermi surface crosses this manifold. Hence, for metals, I mention the Fermi-surface geometry whenever known.

Between these two limiting cases of a weakly doped antiferromagnetic insulator and an antiferromagnetic metal with a large Fermi surface, the experimental manifestations of the Zeeman spin-orbit coupling will be quantitatively different. On top of this, certain effects will be sensitive to the geometry of the degeneracy manifold and its intersection with the Fermi surface, as well as the orientation of the staggered magnetization with respect to the crystal axes. A detailed discussion of these effects will be presented elsewhere.

When selecting the examples below, the preference was given to materials, available in high-purity samples, where de Haas–van Alphen (dHvA) oscillations were observed and where magnetic structure was unambiguously characterized by neutron scattering. As explained in Sec. I, the results of this work apply to materials well inside a long-range antiferromagnetic phase and far enough from any critical point, quantum or classical. For both quantum and thermal fluctuations of antiferromagnetic order to be negligible, the ordered moment shall be noticeable on the scale of the Bohr magneton, and the sample shall be kept well below both the Néel and the effective Fermi temperatures.

A. One dimension

In one dimension, the magnetic Brillouin-zone boundary reduces to two points $\mathbf{p}=\pm\frac{\pi}{2a}$, which in fact coincide up to the antiferromagnetic wave vector $\mathbf{Q}=\frac{\pi}{a}$, that is also a reciprocal-lattice vector of the antiferromagnetic state (see Fig. 5). In terms of the general condition (6), this is the simplest case: $\mathcal{U}=1$.

As a result, at $\mathbf{p}=\pm\frac{\pi}{2a}$, the two exact Bloch states in a transverse field, $|\mathbf{p}\rangle$ and $\theta\mathbf{T_a}\mathbf{U_n}(\pi)|\mathbf{p}\rangle$, correspond to the *same* momentum $\mathbf{p}$ and are degenerate by virtue of $\theta\mathbf{T_a}\mathbf{U_n}(\pi)$ being a symmetry. Equation (5) guarantees their orthogonality, thus protecting the Kramers degeneracy at the momentum $\mathbf{p}=\pm\frac{\pi}{2a}$ against a transverse magnetic field.

B. Two dimensions, rectangular and square symmetries

Now consider a two-dimensional antiferromagnet on a lattice of rectangular or square symmetry with the ordering wave vector $\mathbf{Q}=(\pi,\pi)$. In a transverse magnetic field, the

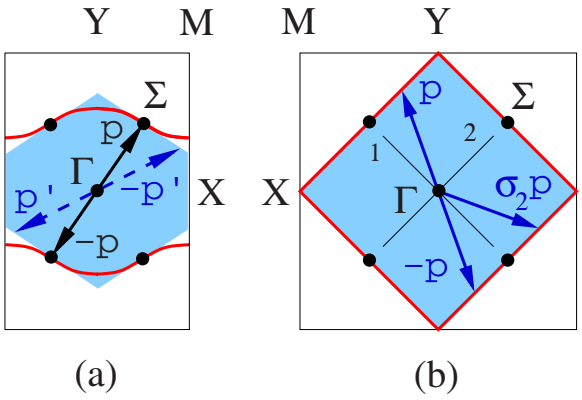

FIG. 6. (Color online) Geometry of the problem. (a) The Brillouin zone for a simple rectangular lattice (the rectangle) and its antiferromagnetic counterpart (MBZ, shaded hexagon). Thick (red) curve, passing through point Σ, shows a typical degeneracy line $g_\perp(\mathbf{p})=0$. At the MBZ boundary, only the momentum $\mathbf{p}$ at point Σ is equivalent to $-\mathbf{p}$ up to a reciprocal-lattice vector of the antiferromagnetic state; for a generic $\mathbf{p}'$, shown by the dashed arrow, this is not true. (b) The Brillouin zone of a simple square lattice and its antiferromagnetic counterpart (shaded diagonal square). The degeneracy line must contain the entire MBZ boundary, shown in red. The point Γ is the Brillouin-zone center, and points X and Y lie at the centers of the paramagnetic Brillouin-zone edges. The point Σ lies at the center of the MBZ boundary.

degeneracy persists on a line in the Brillouin zone by virtue of Eq. (10). I will show that, in the rectangular case, the degeneracy line must contain the point Σ at the center of the MBZ boundary (i.e., the star of $\mathbf{p}=\mathbf{Q}/2$), shown in Fig. 6(a). In the square-symmetry case, the degeneracy persists at the entire MBZ boundary [Fig. 6(b)]. The MBZ in Fig. 6 is the reciprocal-space counterpart of the Wigner-Seitz cell of the magnetic state (Fig. 1), and the ordering wave vector $\mathbf{Q}=(\pi,\pi)$ connects points X and Y in Figs. 6(a) and 6(b).

Consider a Bloch state $|\mathbf{p}\rangle$ at momentum $\mathbf{p}$ in a transverse field. As discussed in Sec. II, the eigenstate $\theta\mathbf{T_a}\mathbf{U_n}(\pi)|\mathbf{p}\rangle$ at momentum $-\mathbf{p}$ is degenerate with $|\mathbf{p}\rangle$ and, according to Eq. (5), must be orthogonal to it unless $(\mathbf{p}\cdot\mathbf{a})$ is an integer multiple of π—put otherwise, unless $\mathbf{p}$ belongs to the paramagnetic Brillouin-zone boundary. At points Σ, X, and Y, momenta $\mathbf{p}$ and $-\mathbf{p}$ coincide up to a reciprocal-lattice vector of the antiferromagnetic state. However, at points X and Y [as well as at the entire vertical segment of the MBZ boundary in Fig. 6(a)], $(\mathbf{p}\cdot\mathbf{a})$ is an integer multiple of π; hence $|\mathbf{p}\rangle$ and $\theta\mathbf{T_a}\mathbf{U_n}(\pi)|\mathbf{p}\rangle$ are not obliged to be orthogonal there as per Eq. (5). Thus, Σ is the only point at the MBZ boundary, where the two degenerate states $|\mathbf{p}\rangle$ and $\theta\mathbf{T_a}\mathbf{U_n}(\pi)|\mathbf{p}\rangle$ are orthogonal and correspond to the *same* momentum. Dashed arrows in Fig. 6(a) show that, for a generic point $\mathbf{p}'$ at the MBZ boundary, no symmetry operation relates $-\mathbf{p}'$ to a vector, equivalent to $\mathbf{p}'$. Therefore, it is only at point Σ that the symmetry protects the Kramers degeneracy against a transverse magnetic field. As in the one-dimensional example of Sec. IV A, in terms of Eq. (6) this corresponds to the simplest case of $\mathcal{U}=1$.

This can be illustrated by a nearest-neighbor hopping spectrum

$$\epsilon_{\mathbf{p}} = t[\cos p_x + \eta \cos p_y] \tag{18}$$

in the weak-coupling example of Sec. III: for the rectangular symmetry ($\eta \neq 1$), the spectrum (10) in a transverse field remains degenerate on a thick (red) line as sketched in Fig. 6(a). Upon variation of $\eta \neq 1$, the line changes its shape, but remains pinned at the star of the wave vector $\mathbf{p}=\mathbf{Q}/2$ (i.e., at the point Σ) in Fig. 6(a). In terms of the Sec. III, the star of $\mathbf{p}=\mathbf{Q}/2$ is the Kramers subset of the degeneracy manifold, while the rest of the degeneracy line in Fig. 6(a) is the accidental degeneracy subset.

Promotion from the rectangular symmetry ($\eta \neq 1$) to that of a square ($\eta=1$) brings along invariance under reflections $\sigma_{1,2}$ in either of the two diagonal axes 1 and 2, passing through point Γ in Fig. 6(b). As a result, the eigenstate $\sigma_1 \theta \mathbf{T}_\mathbf{a} \mathbf{U}_\mathbf{n}(\pi)|\mathbf{p}\rangle$ at momentum $\sigma_2 \mathbf{p}$ [Fig. 6(b)] is also degenerate with $|\mathbf{p}\rangle$ and orthogonal to it, as one can show analogously to the examples above. In terms of the general condition (6), this means $\mathcal{U}=\sigma_{1,2}$.

A momentum $\mathbf{p}$ at the MBZ boundary in Fig. 6(b) differs from $\sigma_2 \mathbf{p}$ by a reciprocal-lattice vector; thus the two momenta coincide in the nomenclature of the antiferromagnetic Brillouin zone. Hence, for a square-symmetry lattice in a transverse field, the degeneracy is of a Kramers (i.e., symmetry-protected) nature at the entire MBZ boundary, as shown in Fig. 6(b). In this case, barring a particularly pathological band structure, the degeneracy manifold is exhausted by its Kramers subset.

In accordance with the symmetry arguments above, for the toy nearest-neighbor hopping spectrum (18) at the square-symmetry point $\eta=1$, the degeneracy line of Eq. (10) coincides with the MBZ boundary, as shown in Fig. 6(b). By contrast, for rectangular symmetry, it is Eq. (10) that restricts the degeneracy in a transverse field to a line in momentum space, and it is the symmetry that pins this line at point Σ at the middle of the MBZ boundary, as shown in Fig. 6(a).

Now, $g_\perp(\mathbf{p})$ can be expanded in a vicinity of the degeneracy line $g_\perp(\mathbf{p})=0$. With the exception of higher-symmetry points, such as point X in Fig. 6(b), the leading term of the expansion is linear in momentum deviation $\delta\mathbf{p}$ from the degeneracy line

$$g_\perp(\mathbf{p}) \approx \frac{\boldsymbol{\Xi}_\mathbf{p} \cdot \delta\mathbf{p}}{\hbar}, \tag{19}$$

where $\boldsymbol{\Xi}_\mathbf{p}/\hbar$ is the momentum gradient of $g_\perp(\mathbf{p})$ at point $\mathbf{p}$ on the degeneracy line. As mentioned in Sec. III A, inversion symmetry makes $g_\perp(\mathbf{p})$ even under inversion. Therefore, $\boldsymbol{\Xi}_\mathbf{p}$ changes sign upon inversion, which is consistent with Eqs. (13) and (16) that require $g_\perp(\mathbf{p})$ to change sign upon momentum shift by $\mathbf{Q}$.

As shown in Sec. III A, $g_\perp(\mathbf{p})$ is an odd function of the deviation $\delta\mathbf{p}$ from the point Σ (the star of $\mathbf{p}=\mathbf{Q}/2$) in Figs. 6(a) and 6(b). Therefore, expansion of $g_\perp(\mathbf{p})$ around the point Σ cannot contain an even power of $\delta\mathbf{p}$.

C. Chromium

This section is devoted to commensurate antiferromagnetism in chromium—the simplest of magnetic orders, occurring in this textbook spin-density wave metal. Chromium crystallizes into a bcc lattice and undergoes various magnetic and structural transitions upon variation of temperature, pressure, or alloying.[1–3]

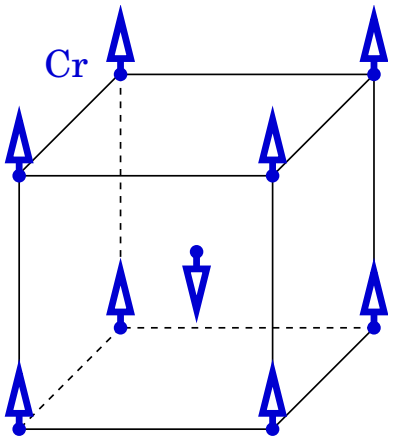

FIG. 7. (Color online) Schematic drawing of the commensurate magnetic structure of antiferromagnetic chromium.

Below the Néel temperature T_N of about 311 K at ambient pressure, chromium develops weakly incommensurate antiferromagnetism with an ordered moment of about $0.5\mu_B$ per atom at 4.2 K. However, strain—or doping with some 0.1–0.3 % of a transition metal [such as Mn, Re, Rh, Ru, Ir, Os, or Pt (Ref. 2)]—eliminates incommensurability in favor of commensurate order with wave vector [001], shown in Fig. 7. Commensurate order has also been observed and much studied in thin films of chromium, often with an enhanced Néel temperature and ordered moment.[18] This paper neglects fluctuations of magnetic order and, conveniently, the high Néel temperature of chromium facilitates experimental access to $T \ll T_N$, where thermal fluctuations are suppressed.

The paramagnetic and the antiferromagnetic Brillouin zones for bulk commensurate antiferromagnetic chromium are shown in Fig. 8(a). An arbitrary momentum at the MBZ boundary becomes equivalent to its opposite upon an appropriate spatial rotation by π. Similarly to the two-dimensional square-symmetry example above, this equivalence is up to a reciprocal-lattice vector of the antiferromagnetic state. Hence, in a transverse magnetic field, the Kramers degeneracy survives at the entire magnetic Brillouin zone boundary in Fig. 8(a).

The disappearance of $g_\perp(\mathbf{p})$ affects the electrons at two different sheets of the Fermi surface, sketched in Fig. 8(b): those at the nearly spherical electron parts, centered at points X in the middle of each MBZ face, and those at the hole ellipsoids, centered at points N in the middle of each MBZ edge. For the former, the leading term of the expansion is linear in the momentum deviation $\delta p_\perp$ from the flat face of the MBZ boundary. For the latter, the leading term of the expansion is quadratic near each MBZ edge, since $g_\perp(\mathbf{p})$ vanishes at each of the two intersecting faces of the MBZ boundary.

D. $CeIn_3$, UIn_3, UGa_3,…

A number of cerium and uranium binary intermetallics of simple-cubic Cu_3Au structure, such as $CeIn_3$, $CeTl_3$, UIn_3,

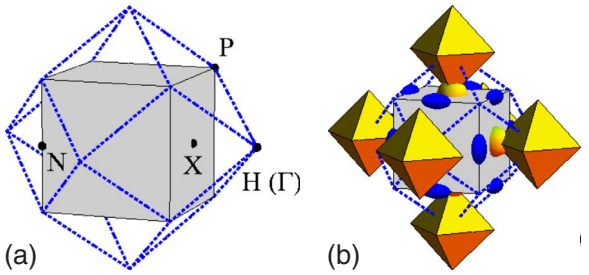

FIG. 8. (Color online) The Brillouin zone and the Fermi surface of commensurate antiferromagnetic chromium. (a) Dashed lines show the paramagnetic Brillouin-zone boundary. The solid cube inside it is the MBZ, with high-symmetry points indicated. In the antiferromagnetic state, the point H is equivalent to the point Γ at the center of the Brillouin zone (not shown). (b) The Fermi-surface sketch of paramagnetic chromium. As in (a), dashed lines show the paramagnetic Brillouin-zone boundary and the solid cube inside it is the MBZ. The nearly octahedral hole Fermi surface is centered at the point H and nearly spherical electron "balls" are located at face centers X of the MBZ boundary. Together with the nearly octahedral electron surface, centered at the point Γ (not shown), these electron balls form the electron "jack." A set of hole ellipsoids is centered at points N in the middle of the magnetic Brillouin-zone edges.

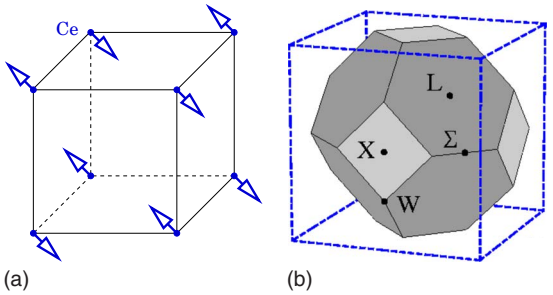

FIG. 9. (Color online) Geometry of $CeIn_3$ in real and in reciprocal space. (a) Cubic unit cell of $CeIn_3$, showing Ce atoms and their magnetic moments. Indium atoms (not shown) are positioned at the face centers of the unit cell. (b) Cubic Brillouin zone of paramagnetic $CeIn_3$ and, inside, its antiferromagnetic counterpart. Darker shading marks the degeneracy surface.

UGa_3, UTl_3, and UPb_3, turn antiferromagnetic at low temperatures. High-purity samples of $CeIn_3$, UIn_3, and UGa_3 have made it possible to characterize the magnetic order and electron properties of these materials rather comprehensively. Some of the basic properties of the samples are shown in Table II.

At low temperature, all three develop a type-II antiferromagnetic structure with wave vector $\mathbf{Q}=[\frac{1}{2}\frac{1}{2}\frac{1}{2}]$, shown in Fig. 9(a) for $CeIn_3$. The materials remain normal metals down to the lowest temperatures probed, with the Sommerfeld coefficient substantially enhanced by comparison to that of a simple metal (see the fourth column of Table II versus about 0.65 $\mathrm{mJ/K^2}$ mol for Ag).

Of the three materials, $CeIn_3$ has been scrutinized the most. Its early studies were driven by interest in valence[29] and magnetic[19] fluctuations, in the nature of its magnetic order,[19] in large mass enhancement[30] and related questions. Subsequent research focused on the reduction of T_N under pressure and on superconductivity, discovered near the critical pressure p_c, where the Néel temperature is about to vanish—as well as on marked departure from Landau Fermi-liquid behavior, found in the normal state near p_c.[22,31,32] The most recent work included de Haas–van Alphen oscillation measurements,[21,33] electron-positron annihilation experiments,[34] and interpretation of the former.[35]

According to Fig. 9(b), the magnetic Brillouin zone of the three metals enjoys full cubic symmetry. Its square faces belong to the paramagnetic Brillouin-zone boundary $(\mathbf{p}\cdot\mathbf{a})=\pm\pi$, where Eq. (5) does not enforce degeneracy; however, $g_\perp(\mathbf{p})$ does vanish at the hexagonal MBZ faces, marked by darker shading in Fig. 9(b).

According to de Haas–van Alphen measurements[21,36] and to calculations,[37] one sheet of the Fermi surface of $CeIn_3$ is nearly spherical and has a radius of about $\frac{\pi}{a}\frac{\sqrt{3}}{2}$, where a is the lattice constant. Hence this sheet comes close to the point L in Fig. 9(b), which is the very same distance $\frac{\pi}{a}\frac{\sqrt{3}}{2}$ away from the Brillouin-zone center. Disappearance of $g_\perp(\mathbf{p})$ necessarily affects the dynamics of an electron on this sheet in a transverse field.

Near a generic point at an MBZ face, far from its edges, leading terms of the expansion of $g_\perp(\mathbf{p})$ are linear in transverse deviation of momentum from the MBZ face as per Eq. (19), with $\boldsymbol{\Xi}_\mathbf{p}$ normal to the MBZ boundary. Near the edges, joining the neighboring hexagonal faces in Fig. 9(b)—for instance, near the points Σ and W—the leading terms become quadratic.

E. Uranium nitride

Uranium nitride (UN) presents another example of interest. This heavy fermion metal has a face-centered cubic lat-

TABLE II. Simple properties of some of the studied samples of $CeIn_3$, UGa_3, and UIn_3: the Néel temperature T_N, the ordered magnetic moment M, the Sommerfeld coefficient γ, the residual resistivity ρ_0, and the residual resistivity ratio $\rho(300\ \mathrm{K})/\rho_0$.

Material	T_N (K)	M (μ_B)	γ ($\mathrm{mJ/K^2}$ mol)	ρ_0 ($\mu\Omega$ cm)	$\frac{\rho(300\ \mathrm{K})}{\rho_0}$
$CeIn_3$	10.1	0.5/Ce[19]	130[20]	0.5[20]	35[20]
				0.6[21]	100[22]
UGa_3	64[23]	0.75/U[23]	52[24–26]	1.2[26]	38[25]
					81[26]
UIn_3	88	1/U[27]	50[24]	0.66[28]	130[28]

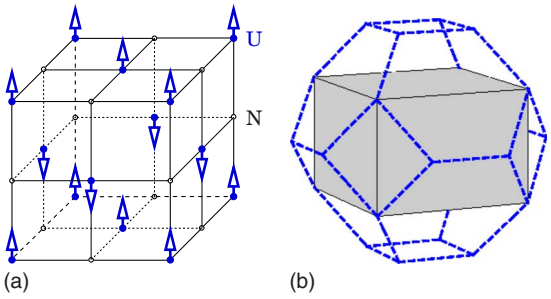

FIG. 10. (Color online) Geometry of UN in real and in reciprocal spaces. (a) Fcc cubic unit cell of UN, showing U atoms and their magnetic moment orientation. Nitrogen atoms are shown by open circles. (b) Dashed lines define the Brillouin-zone boundary of paramagnetic UN; the square prism inside it is the antiferromagnetic Brillouin zone. Its entire boundary defines the degeneracy surface $g_{\perp}(\mathbf{p})=0$.

tice of NaCl type, shown in Fig. 10(a). Below 53 K, it develops type-I antiferromagnetic order, with ordered moment of about $0.75\mu_B$ per uranium atom,[38] and Sommerfeld coefficient of 50 $\mathrm{mJ/K^2}$ mol.[39] The Néel temperature of UN drops under pressure, vanishing at about 3.5 GPa. Recent experiments[39] studied the low-temperature resistivity near the critical pressure on samples with residual resistivity ρ_0 of about 2.3 $\mu\Omega$ cm and the residual resistivity ratio $\rho(300\ \mathrm{K})/\rho_0$ of the order of 10^2.

The real-space sketch of magnetic structure of UN is shown in Fig. 10 together with its paramagnetic and antiferromagnetic Brillouin-zone boundaries. The MBZ has full tetragonal symmetry and, in a transverse field, all the states at its boundary retain Kramers degeneracy. The leading terms in the expansion of $g_{\perp}(\mathbf{p})$ are linear near the MBZ faces, quadratic near the edges, and cubic near the vertices.

F. $CePd_2Si_2$ and $CeRh_2Si_2$

The heavy fermion metal $CePd_2Si_2$ has a body-centered tetragonal structure of $ThCr_2Si_2$ type, shown in Fig. 11(a). It is isostructural to $CeCu_2Si_2$—the first discovered heavy fermion superconductor[40]—and $CeCu_2Ge_2$, an incommensurate antiferromagnet[41] that becomes superconducting above 70 kbar in a pressure cell.[42]

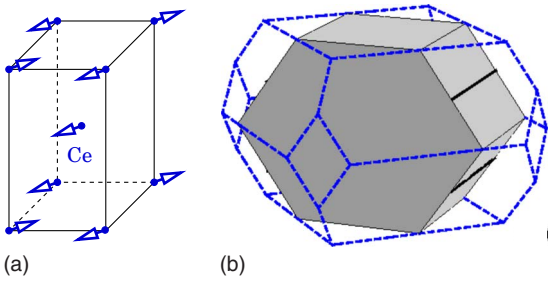

FIG. 11. (Color online) Geometry of $CePd_2Si_2$ in real and in reciprocal space. (a) Tetragonal unit cell of $CePd_2Si_2$ showing Ce atoms and the orientation of their magnetic moments. A full sketch, showing Pd and Si atoms, is given in Ref. 45. (b) The Brillouin-zone boundary of paramagnetic $CePd_2Si_2$ is shown by dashed lines. The shaded hexagonal prism is its antiferromagnetic counterpart.

Below about 10 K, $CePd_2Si_2$ orders antiferromagnetically as shown in Fig. 11(a), with wave vector $\mathbf{Q}=[\frac{1}{2}\frac{1}{2}0]$, and a low-temperature ordered moment of about $0.7\mu_B$ per Ce atom. Its Sommerfeld coefficient is enhanced to about 100 $\mathrm{mJ/K^2}$ mol. Samples of the present generation show residual resistivity in the $\mu\Omega$ cm range.[22] Under hydrostatic pressure of 26 kbar, the Néel temperature drops to under 1 K and, in a pressure window of ± 5 kbar around this value, superconductivity appears, with a maximum transition temperature of about 0.4 K.[43] Curiously enough, the normal-state resistivity near this pressure follows a temperature dependence that does not fit the $\rho(T)=\rho_0+AT^2$ temperature dependence of the Landau Fermi-liquid theory, but instead behaves as $\rho(T)\sim T^{1.2}$ over more than a decade in temperature between about 1 and 40 K.[43]

The unit cell of $CePd_2Si_2$ and its paramagnetic and antiferromagnetic Brillouin-zone boundaries are shown in Fig. 11. By symmetry, the degeneracy manifold in a transverse field includes the two hexagonal faces of the MBZ boundary, one of which is shown by darker shading in Fig. 11(b), and the four one-dimensional segments, two of which are shown in black. Along these segments, which are a one-dimensional analog of the point Σ in Fig. 6(a), another sheet of the degeneracy surface may cross the side faces of the MBZ. According to de Haas–van Alphen experiments,[44] several Fermi-surface sheets cross the degeneracy surface. The leading term in the expansion of $g_{\perp}(\mathbf{p})$ around the hexagonal MBZ faces is linear.

$CeRh_2Si_2$ is an isostructural relative of $CePd_2Si_2$, with a modestly enhanced Sommerfeld coefficient of about 23 $\mathrm{mJ/K^2}$ mol. Between $T_{N1}\approx 36$ K and $T_{N2}\approx 25$ K, it develops Néel order with $\mathbf{Q}=[\frac{1}{2}\frac{1}{2}0]$.[45,46] Magnetic structure below T_{N2} has not yet been established unambiguously.[45,46] Both T_{N1} and T_{N2} drop under pressure[47] and, in an extended pressure window above 5 kbar, $CeRh_2Si_2$ becomes superconducting at a T_c with a maximum of about 0.5 K.[48] Antiferromagnetic structure of $CeRh_2Si_2$ between T_{N1} and T_{N2} coincides with that of $CePd_2Si_2$, as does the degeneracy surface in Fig. 11(b). According to Ref. 49, at least one sheet of the Fermi surface of $CeRh_2Si_2$ crosses the degeneracy surface or comes close to it.

G. Neodymium hexaboride

Rare earth hexaborides RB_6 are an interesting family, whose members show diverse electron and magnetic properties. Of the (relatively) simple ones, LaB_6 is a diamagnetic metal and SmB_6 is a mixed-valence semiconductor. Of the ordered materials, EuB_6 is a ferromagnetic semimetal and CeB_6 is a heavy fermion metal with at least two ordered phases, whose nature remains to be elucidated after nearly 40 years of research.

Three members of the family, NdB_6, GdB_6, and PrB_6, are antiferromagnetic at low temperature. In PrB_6 (Ref. 50) and in GdB_6 (Refs. 51 and 52) alike, two different low-temperature antiferromagnetic states have been found.

Neodymium hexaboride NdB_6 presents a simpler picture: below about 8 K, it is a collinear type-I antiferromagnet with ordering vector $\mathbf{Q}=[00\frac{1}{2}]$ and an ordered moment of about

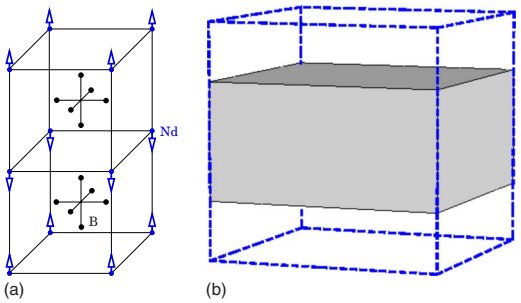

FIG. 12. (Color online) Neodymium hexaboride. (a) Crystalline and magnetic structures of NdB_6: a CsCl structure with B octahedra replacing Cl atoms and Nd in place of Cs. The arrows show magnetic moments of neodymium atoms. (b) Dashed lines show the cubic Brillouin zone of paramagnetic NdB_6. The shaded square prism inside it is the tetragonal Brillouin-zone boundary in the antiferromagnetic state. Its darker face denotes the degeneracy plane.

$1.74\mu_B$;[53] antiferromagnetism doubles its cubic unit cell in the [0 0 1] direction, as shown in Fig. 12(a). Thus the cubic magnetic Brillouin zone reduces by half in the [0 0 1] direction, while keeping its other two dimensions intact, as shown in Fig. 12(b).

In a transverse field, the Kramers degeneracy is protected at the two faces of the MBZ boundary, one of which is shown by darker shading in Fig. 12(b). According to de Haas–van Alphen measurements[54,55] and to calculations,[56] at least one sheet of the Fermi surface crosses the degeneracy surface. Recently studied samples had residual resistivities well below $\mu\Omega$ cm and residual resistivity ratios of over a 100.[54,57]

H. Other materials of interest

This section contains a brief discussion of other antiferromagnets, where symmetry may protect the degeneracy of special electron states against transverse magnetic field, giving rise to Zeeman spin-orbit coupling (1).

1. Cuprate superconductors

Electron-doped cuprates such as $Nd_{2-x}Ce_xCuO_{4\pm\delta}$ develop commensurate antiferromagnetic order in a wide range of doping,[58] albeit with a modest staggered moment.[59] For such materials, Fig. 6(b) describes the paramagnetic and antiferromagnetic Brillouin-zone boundaries. Angle-resolved photoemission experiments[60] on $Nd_{2-x}Ce_xCuO_{4\pm\delta}$ have found carriers near the MBZ boundary. In a transverse magnetic field, these carriers are subject to Zeeman spin-orbit coupling (1), provided antiferromagnetism in the sample is developed well enough.

Recent observation[61] of magnetic oscillations in $YBa_2Cu_3O_{6.5}$ testifies to great progress in the sample quality of cuprates. The fact that this and other underdoped cuprates are, at the very least, close to commensurate antiferromagnetism makes them an interesting opportunity to examine the effects of Zeeman spin-orbit coupling.

2. Borocarbides

Borocarbides RT_2B_2C with R=Sc, Y, La, Th, Dy, Ho, Er, Tm, or Lu and T=Ni, Ru, Pd, or Pt have been a subject of active research, driven by interest in interplay between antiferromagnetism and superconductivity.[4] At low temperatures, commensurate antiferromagnetism develops in a number of borocarbides (for instance, in RNi_2B_2C with R=Pr, Dy, or Ho), often with a large staggered moment ($\approx 8.5\mu_B$ for Dy and Ho).[4] Zeeman spin-orbit coupling (1) is active whenever a sheet of the Fermi surface crosses the degeneracy manifold, and successful growth of high-quality single crystals[62] makes these materials an interesting case to study.

3. Organic conductors

Organic conductors are an immense and ever growing class of materials, that show virtually all known types of electron states, found in condensed-matter physics.[8] Antiferromagnetism appears in several families of organic conductors, and manifestations of Zeeman spin-orbit coupling (1) are likely to be found in some of them.

Unfortunately, so far nearly all of the information on magnetic structure of organic antiferromagnets has been coming from indirect probes such as magnetic susceptibility measurements[63,64] and resonance spectroscopies.[65–67] Neutron diffraction studies are hampered by a typically small ordered moment and by the difficulties of growing large enough single-crystalline samples. At the moment of writing, I am aware of only a single cycle of neutron-scattering experiments[68–70] on an organic conductor. Moreover, in families such as $(TMTSF)_2$ Bechgaard salts[8] and κ-$(BEDT\text{-}TTF)_2X$ salts,[71,72] antiferromagnetic states are insulating and their controlled doping remains a challenge.[73]

With this word of caution, a number of organic conductors may deserve attention. Semimetallic Bechgaard salt $(TMTSF)_2NO_3$,[74] developing a spin-density wave state below about 9 K, may be one interesting case. Recently synthesized ethylenedioxytetrathiafulvalenoquinone-1,3-diselenolemethide (EDO-TTFVODS), that appears to turn antiferromagnetic below about 4.5 K and remains normal down to the lowest studied temperature of 0.45 K,[75] may be another. Finally, recent studies[76–78] of $[Au(tmdt)_2]$, where tmdt denotes trimethylenetetrathiafulvalenedithiolate, draw attention to this organic conductor. Albeit the material is not yet fully characterized and its large single crystals remain difficult to grow, it appears to have a Néel temperature of about 110 K,[77,78] which is anomalously high for an organic material—and shows normal conduction down to at least 10 K.

4. Heavy fermion materials

Several heavy fermion antiferromagnets were reviewed in detail above. A number of other interesting examples may be found in Ref. 10.

5. Gadolinium antiferromagnets

Gadolinium antiferromagnets (see Refs. 79 and 80 and Table 1 in Ref. 81) offer two important advantages for an experimental study of the Zeeman spin-orbit coupling. First, their often elevated Néel temperature T_N (such as 134 K for GdAg or 150 K for GdCu) facilitates experimental access to temperatures well below T_N, where thermal fluctuations of

antiferromagnetic order are frozen out. Second, large ordered moment of these materials (about $7.5\mu_B$ for GdAg and about $7.2\mu_B$ for $GdCu_2Si_2$) quenches quantum fluctuations. Therefore, gadolinium antiferromagnets fit well into the present framework with its neglect of both quantum and classical fluctuations—and shall be convenient for a study of various effects of the Zeeman spin-orbit coupling.

6. Iron pnictides

Iron pnictides have been attracting immense attention[82] due to appearance of commensurate antiferromagnetism[7] and high-temperature superconductivity[83] in this copper-free family of materials. Combination of commensurate antiferromagnetism[7] with essentially metallic normal-state conduction[83,84] not only contrasts iron pnictides with the cuprates (that are believed to be Mott insulators), but also makes the former materials likely to manifest a substantial momentum dependence of the g-tensor.

V. DISCUSSION

A. Effects of the intrinsic spin-orbit coupling

The arguments above appealed to the exchange symmetry approximation:[17] the point symmetry operations of the electron Hamiltonian in an antiferromagnet were considered inert with respect to spin, and the intrinsic relativistic spin-orbit coupling, that appears in the absence of an external magnetic field, was thus neglected. I will now examine the effects it may have.

First, this spin-orbit interaction generates magnetic anisotropy that creates a preferential orientation of the staggered magnetization $\mathbf{n}$ with respect to the crystal axes. In an experiment, this allows one to vary the magnetic field orientation with respect to $\mathbf{n}$ as long as the field remains below the reorientation threshold.

At the same time, the spin-orbit coupling may eliminate those spatial symmetries that rotate the magnetization density with respect to the lattice. For instance, certain spin rotations and spatial transformations, that were independent symmetries within the exchange symmetry approximation, may survive only when combined. I will now illustrate this by two examples of Sec. IV.

A simple case of the spin-orbit coupling affecting the Kramers degeneracy manifold in a transverse field is given by a two-dimensional antiferromagnet on a square-symmetry lattice as in Fig. 6(b). Here, the Kramers degeneracy at the antiferromagnetic Brillouin-zone boundary relies, everywhere except for points Σ, on the symmetry with respect to reflections in diagonal planes 1 and 2. If either of these reflections changes the orientation of $\mathbf{\Delta_r}$ with respect to the crystal axes, the spin-orbit coupling may lift the degeneracy at a relevant part of the magnetic Brillouin-zone boundary, except for points Σ. However, if the magnetization density points along one of these diagonal axes, the degeneracy survives at the two faces of the MBZ boundary that are normal to this axis.

In the case of commensurate order in chromium, consider a single-domain sample with magnetic structure shown in Fig. 7. For a Bloch state $|\mathbf{p}\rangle$ with a momentum $\mathbf{p}$ at one of the two horizontal faces of the magnetic Brillouin zone in Fig. 8(a), the degenerate partner state $\theta\mathbf{T_a}\mathbf{U_n}(\pi)|\mathbf{p}\rangle$ has momentum $-\mathbf{p}$ at the other horizontal face of the MBZ. The coordinate rotation by π around the vertical symmetry axis, passing through the center Γ of the Brillouin zone, transforms the momentum $\mathbf{p}$ into $\mathbf{p}+\mathbf{Q}$, equivalent to $\mathbf{p}$ up to the reciprocal-lattice vector $\mathbf{Q}$ of the antiferromagnetic state.

By contrast, for a momentum $\mathbf{p}$ at one of the vertical faces of the MBZ, a coordinate rotation by π around a horizontal axis is required. Such a rotation inverts $\mathbf{\Delta_r}$ once the latter is attached to the crystal axes. Thus spin-orbit coupling tends to lift the degeneracy at the vertical faces of the MBZ, leaving it intact at the two horizontal faces. The other examples of Sec. IV can be analyzed similarly. Finally, those spin-orbit coupling terms that act directly on the electron spin and tend to lift the double degeneracy of Bloch eigenstates even in the absence of magnetic field were neglected here altogether.

B. Relation to earlier work

When symmetries of a system involve time reversal—alone or in combination with other operations—a proper treatment must involve nonunitary symmetry groups: those containing unitary as well as antiunitary elements. In this case, construction of irreducible representations is complicated by the fact that antiunitary elements involve complex conjugation. In a group representation, combination of two unitary elements u_1 and u_2 is represented by the product of the corresponding matrices $\mathbf{D}(u_1)$ and $\mathbf{D}(u_2)$ as per $\mathbf{D}(u_1u_2)=\mathbf{D}(u_1)\mathbf{D}(u_2)$. By contrast, combination of an antiunitary element a with a unitary element u involves complex conjugation: $\mathbf{D}(au)=\mathbf{D}(a)\mathbf{D}^*(u)$. As a result, irreducible representations of a nonunitary group must include a unitary representation and its complex conjugate on an equal footing. Discussion of such representations (called corepresentations) was given by Wigner,[85] along with the analysis of arising possibilities with the help of the Frobenius-Schur criterion. Later, Herring[86] studied spectral degeneracies emerging in crystals due to time-reversal symmetry and, among other things, extended this criterion to space groups. In a subsequent work, Dimmock and Wheeler[13] generalized the criterion further, to magnetic crystals, and pointed out the sufficient condition (6) for the appearance of extra degeneracies.

The present work identifies the symmetry, that protects the Kramers degeneracy in a Néel antiferromagnet against transverse magnetic field, as a conspiracy between the antiunitary symmetry $\mathbf{U_n}(\pi)\mathbf{T_a}\theta$, inherent to any collinear commensurate antiferromagnet in a transverse field, and the crystal symmetry of those special momenta at the MBZ boundary, that are defined by Eq. (6). Formally, the present work is an extension of Ref. 13 since one may think of the last two terms in Eq. (4) as of the exchange field of a fictitious magnetic crystal in zero field. However, Kramers degeneracy in a magnetic field has rather special and remarkable experimental signatures, some of which are outlined at the end of the section V C.

Last but not the least, Ref. 14 was an important source of inspiration for the present work. Its authors studied the elec-

tron eigenstates in a Néel antiferromagnet on a lattice of square symmetry and, for this particular case, pointed out the disappearance of $g_\perp(\mathbf{p})$ at the MBZ boundary, as well as the ensuing substantial momentum dependence of $g_\perp$ in the Zeeman coupling (1). The present paper builds on Ref. 14 by elucidating the structure of the manifold of degenerate states for an arbitrary crystal symmetry and for an arbitrary transverse field that can be sustained by the antiferromagnet before its sublattices collapse. This is to be contrasted with the analysis of Ref. 14, performed to the linear order in the field. Several other aspects of Ref. 14 are discussed in Appendix D.

C. Experimental signatures

The Kramers degeneracy at special momenta on the MBZ boundary and the resultant Zeeman spin-orbit coupling have a number of interesting consequences. For instance, a substantial momentum dependence of $g_\perp(\mathbf{p})$ in Eq. (1) means that, generally, the electron-spin resonance (ESR) frequency of a carrier in the vicinity of the degeneracy manifold varies along the quasiclassical trajectory in momentum space.

For a weakly doped antiferromagnetic insulator with a conduction-band minimum on the degeneracy manifold, this leads to an inherent broadening of the ESR line with doping and, eventually, complete loss of the ESR signal. In fact, this may well be the reason behind the long-known "ESR silence"[87] of the cuprates. Suppression of the Pauli paramagnetism in the transverse direction with respect to staggered magnetization is another simple consequence of vanishing $g_\perp(\mathbf{p})$.

At the same time, a momentum dependence of $g_\perp(\mathbf{p})$ allows excitation of spin-resonance transitions by ac *electric* rather than magnetic field[88,89]—a vivid effect of great promise for controlled spin manipulation, currently much sought after in spin electronics. Its absorption matrix elements are defined by $\boldsymbol{\Xi}_\mathbf{p}$ of Eq. (19). Comparison to Eq. (11) shows that, within the weak-coupling model (8), $\boldsymbol{\Xi}_\mathbf{p}/\hbar$ is of the order of the antiferromagnetic coherence length $\xi \sim \frac{\hbar v_F}{\Delta}$ and may be of the order of the lattice period or much greater. By contrast, the ESR matrix elements are defined by the Compton length $\lambda_C = \frac{\hbar}{mc} \approx 0.4$ pm. Thus, the matrix elements of electrically excited spin transitions exceed those of ESR by about $\frac{\hbar c}{e^2}\frac{\epsilon_F}{\Delta} \approx 137\frac{\epsilon_F}{\Delta}$, i.e., at least by 2 orders of magnitude. Being proportional to the square of the appropriate transition matrix element, resonance absorption due to electric excitation of spin transitions exceeds that of ESR at least by 4 orders of magnitude. Last but not the least, according to Eq. (19), resonance absorption in this phenomenon shows a nontrivial dependence on the orientation of the ac electric field with respect to the crystal axes, and on the orientation of the dc magnetic field with respect to the staggered magnetization.

The Zeeman spin-orbit coupling may also manifest itself in other experiments on antiferromagnetic conductors. In particular, de Haas–van Alphen oscillations[90] and magneto-optical response may be modified. In various types of electron response, interesting effects may arise due to an extra term $\mathbf{v}_{\mathrm{ZSO}}$ in the electron velocity operator, emerging due to a substantial momentum dependence of $g_\perp(\mathbf{p})$ in Eq. (1)

$$\mathbf{v}_{\mathrm{ZSO}} = \nabla_\mathbf{p}\mathcal{H}_{\mathrm{ZSO}} = -\mu_B \nabla_\mathbf{p} g_\perp(\mathbf{p})(\mathbf{H}_\perp \cdot \boldsymbol{\sigma}). \tag{20}$$

This term describes spin current. However, $g_\perp(\mathbf{p})$ is even in $\mathbf{p}$ due to inversion symmetry and thus, in equilibrium, the net spin current must vanish. This may change if the system were tilted, say, by electric current or otherwise, however, the resulting effect would be proportional to the "tilt" and, in addition to this, would be small in the measure of $H_\perp/\Delta$.

D. Conclusions

In this work, I studied the degeneracy of electron Bloch states in a Néel antiferromagnet, subject to a transverse magnetic field, and described the special points in momentum space, where the degeneracy is protected by a hidden antiunitary symmetry.

I discussed the simplest properties and some of the manifestations of the Zeeman spin-orbit coupling, arising in a magnetic field due to this degeneracy, and outlined several examples of interesting materials, where such a coupling may be active. Finally, I reviewed the results and their relation to earlier work.

The degeneracy of special Bloch states in a transverse field hinges only on the symmetry of the antiferromagnetic state and thus holds in weakly coupled and strongly correlated materials alike—provided long-range antiferromagnetic order and well-defined electron quasiparticles are present. Under these conditions, thermal and quantum fluctuations of the antiferromagnetic order primarily renormalize the sublattice magnetization, leaving intact the degeneracy of special electron states in a transverse field—certainly in the leading order in fluctuations. Detailed account of fluctuations is outside the scope of this paper.

ACKNOWLEDGMENTS

I am indebted to S. Brazovskii and G. Shlyapnikov for inviting me to Orsay, to LPTMS for the kind hospitality, and to IFRAF for the generous support. I am grateful to S. Brazovskii, M. Kartsovnik, and K. Kanoda for references on organic antiferromagnets and to C. Capan for drawing my attention to gadolinium compounds. It is my pleasure to thank S. Carr, N. Cooper, N. Shannon, and M. Zhitomirsky for their helpful comments on the paper, and A. Chubukov and G. Volovik for enlightening discussions.

APPENDIX A: ORTHOGONALITY RELATION

This Appendix proves the relation

$$\langle\phi|[\mathcal{O}\theta]^+|[\mathcal{O}\theta]|\psi\rangle = \langle\psi|\phi\rangle, \tag{A1}$$

where $|\phi\rangle$ and $|\psi\rangle$ are arbitrary states, $\mathcal{O}$ is an arbitrary unitary operator, and θ is time reversal. In the main text, this relation is used for $|\phi\rangle = \mathcal{O}\theta|\psi\rangle$; in this case, when read right to left, Eq. (A1) yields

$$\langle\psi|\mathcal{O}\theta|\psi\rangle = \langle\psi|[(\mathcal{O}\theta)^+]^2|(\mathcal{O}\theta)|\psi\rangle. \tag{A2}$$

Whenever $|\psi\rangle$ is an eigenvector of the linear operator $[\mathcal{O}\theta]^2$ with an eigenvalue different from unity, Eq. (A2) proves orthogonality of $|\psi\rangle$ and $\mathcal{O}\theta|\psi\rangle$.

The proof of Eq. (A1) is based on the obvious relation $(\mathcal{C}\phi,\mathcal{C}\psi)=(\psi,\phi)$ for arbitrary complex vectors ϕ and ψ, where $(\psi,\phi)\equiv\Sigma_i\psi_i^*\phi_i$ denotes scalar product and $\mathcal{C}$ is complex conjugation. Hence, for an arbitrary unitary operator $\mathcal{O}$, one finds $(\mathcal{OC}\phi,\mathcal{OC}\psi)=(\psi,\phi)$ due to invariance of scalar product under unitary transformation. Time reversal θ can be presented as a product of $\mathcal{C}$ and a unitary operator:[85] $\theta=\mathcal{VC}$, thus $\mathcal{C}=\mathcal{V}^{-1}\theta$ and, therefore, $(\mathcal{O}\theta\phi,\mathcal{O}\theta\psi)=(\psi,\phi)$. As a result, for arbitrary states $|\psi\rangle$ and $|\phi\rangle$, one finds $\langle\phi|[\mathcal{O}\theta]^+|[\mathcal{O}\theta]|\psi\rangle=\langle\psi|\phi\rangle$, which indeed amounts to Eq. (A1).

APPENDIX B: CANTING OF THE SUBLATTICES

Canting of the two sublattices by a transverse field $\mathbf{H}_\perp$ induces a component $\mathbf{\Delta}_\mathbf{r}^\perp$ of the magnetization density along the field, with the periodicity of the underlying lattice, $\mathbf{\Delta}_{\mathbf{r}+\mathbf{a}}^\perp(H_\perp)=\mathbf{\Delta}_\mathbf{r}^\perp(H_\perp)$, as shown in Fig. 3. As a result, the diagonal part of the Hamiltonian (8) acquires an additional term $(\mathbf{\Delta}_\mathbf{p}^\perp\cdot\boldsymbol{\sigma})$, and Hamiltonian (8) thus takes the form

$$\mathcal{H}=\begin{bmatrix}\epsilon_\mathbf{p}-(\tilde{\mathbf{\Delta}}_\mathbf{p}^\perp\cdot\boldsymbol{\sigma}) & (\mathbf{\Delta}_\parallel\cdot\boldsymbol{\sigma})\\ (\mathbf{\Delta}_\parallel\cdot\boldsymbol{\sigma}) & \epsilon_{\mathbf{p}+\mathbf{Q}}-(\tilde{\mathbf{\Delta}}_{\mathbf{p}+\mathbf{Q}}^\perp\cdot\boldsymbol{\sigma})\end{bmatrix}, \tag{B1}$$

where $\tilde{\mathbf{\Delta}}_\mathbf{p}^\perp\equiv\mathbf{H}_\perp+\mathbf{\Delta}_\mathbf{p}^\perp$.

The same choice of spin axes as in Sec. III splits the Hamiltonian (B1) into two independent pieces

$$\mathcal{H}_{1(2)}=\begin{bmatrix}\epsilon_\mathbf{p}\mp\tilde{\Delta}_\mathbf{p}^\perp & \Delta_\parallel\\ \Delta_\parallel & \epsilon_{\mathbf{p}+\mathbf{Q}}\pm\tilde{\Delta}_{\mathbf{p}+\mathbf{Q}}^\perp\end{bmatrix}. \tag{B2}$$

As in Sec. III A, the momentum boost by $\mathbf{Q}$ maps $\mathcal{H}_1$ and $\mathcal{H}_2$ onto each other, and the spectral symmetries of Hamiltonian (B1) coincide with those discussed in Sec. III A. Thus all of the conclusions of Sec. III remain valid after the sublattice canting is accounted for.

However, while the degeneracy at the special points is protected by symmetry, the shape of the manifold of degenerate states may change under various perturbations. For instance, sublattice canting in a transverse field modifies the equation, describing this manifold and, for the conduction band, turns it into

$$\psi_\mathbf{p}+\frac{\phi_\mathbf{p}\zeta_\mathbf{p}}{\sqrt{\Delta_\parallel^2+\phi_\mathbf{p}^2+\zeta_\mathbf{p}^2}}=0 \tag{B3}$$

where $\phi_\mathbf{p}\equiv\frac{1}{2}[\tilde{\Delta}_\mathbf{p}^\perp+\tilde{\Delta}_{\mathbf{p}+\mathbf{Q}}^\perp]$ and $\psi_\mathbf{p}\equiv\frac{1}{2}[\tilde{\Delta}_\mathbf{p}^\perp-\tilde{\Delta}_{\mathbf{p}+\mathbf{Q}}^\perp]$. Since $\mathbf{\Delta}_\mathbf{r}^\perp$ has the real-space periodicity of the paramagnetic state, $\tilde{\Delta}_\mathbf{p}^\perp$ enjoys the same reciprocal space symmetry as $\epsilon_\mathbf{p}$. In particular, $\tilde{\Delta}_{\mathbf{p}+2\mathbf{Q}}^\perp=\tilde{\Delta}_\mathbf{p}^\perp$ and $\tilde{\Delta}_\mathbf{p}^\perp=\tilde{\Delta}_{-\mathbf{p}}^\perp$ (the latter property is also protected by the $\mathbf{U}_\mathbf{l}(\pi)\theta$ symmetry). At the same time, $\psi_{\mathbf{p}+\mathbf{Q}}=-\psi_\mathbf{p}$ and $\phi_{\mathbf{p}+\mathbf{Q}}=\phi_\mathbf{p}$; thus the symmetry-dictated degeneracy points such as $\mathbf{p}=\frac{\mathbf{Q}}{2}$ explicitly belong to the manifold of Eq. (B3), as they should.

In the limit of vanishing $H_\perp$, $\tilde{\Delta}_\mathbf{p}^\perp$ is linear in the field: $\tilde{\Delta}_\mathbf{p}^\perp=H_\perp[1+\chi_\mathbf{p}^\perp]$, where $\chi_\mathbf{p}^\perp$ describes microscopic transverse susceptibility of the antiferromagnet. Now one may expand Eq. (B3) to the linear order in the field to obtain the following equation for the degeneracy manifold:

$$\chi_\mathbf{p}^-+\frac{\chi_\mathbf{p}^+\zeta_\mathbf{p}}{\sqrt{\Delta_\parallel^2+\zeta_\mathbf{p}^2}}=0, \tag{B4}$$

where $\chi_\mathbf{p}^\pm\equiv\chi_\mathbf{p}\pm\chi_{\mathbf{p}+\mathbf{Q}}$. Compared to the equation $\zeta_\mathbf{p}=0$ of Sec. III, the sublattice canting affects the degeneracy manifold already in the zeroth order in $H_\perp$.

APPENDIX C: DIMENSIONALITY OF THE DEGENERACY MANIFOLD

The dimensionality of the degeneracy manifold in a transverse field is one less than that of the momentum space for simple reasons that rely only on the symmetry of the antiferromagnetic state. According to Eq. (3), zero-field Bloch eigenstates $|1\rangle\equiv|\mathbf{p}\rangle$ and $|2\rangle\equiv\mathcal{I}\mathbf{T}_\mathbf{a}\theta|\mathbf{p}\rangle$ form a Kramers doublet at momentum $\mathbf{p}$. Its splitting $\delta\mathcal{E}(\mathbf{p})$ in a transverse field $\mathbf{H}_\perp$ is given by

$$\delta\mathcal{E}(\mathbf{p})=2\sqrt{|V_{12}(\mathbf{p})|^2+\frac{1}{4}[V_{11}(\mathbf{p})-V_{22}(\mathbf{p})]^2}, \tag{C1}$$

where $V_{ij}(\mathbf{p})\equiv\langle i|(\mathbf{H}_\perp\cdot\boldsymbol{\sigma})|j\rangle$. Magnetic field being uniform, $(\mathbf{H}_\perp\cdot\boldsymbol{\sigma})$ commutes with $\mathcal{I}\mathbf{T}_\mathbf{a}$; it also changes sign under time reversal. Thus, $V_{22}(\mathbf{p})=-V_{11}(\mathbf{p})$. At the same time, the off-diagonal matrix element $V_{12}(\mathbf{p})$ vanishes identically

$$\begin{aligned}\langle\mathbf{p}|(\mathbf{H}_\perp\cdot\boldsymbol{\sigma})\mathcal{I}\mathbf{T}_\mathbf{a}\theta|\mathbf{p}\rangle&=\sum_\mathbf{q}\langle\mathbf{p}|(\mathbf{H}_\perp\cdot\boldsymbol{\sigma})|\mathbf{q}\rangle\langle\mathbf{q}|\mathcal{I}\mathbf{T}_\mathbf{a}\theta|\mathbf{p}\rangle\\&=\sum_\mathbf{q}V_{11}(\mathbf{p})\delta_{\mathbf{pq}}\langle\mathbf{q}|\mathcal{I}\mathbf{T}_\mathbf{a}\theta|\mathbf{p}\rangle=V_{11}(\mathbf{p})\langle\mathbf{p}|\mathcal{I}\mathbf{T}_\mathbf{a}\theta|\mathbf{p}\rangle\equiv 0,\end{aligned} \tag{C2}$$

where insertion of unity $1=\Sigma_\mathbf{q}|\mathbf{q}\rangle\langle\mathbf{q}|$ was used in the first line, uniformity of $\mathbf{H}_\perp$ in the second, and the final equality followed from Eq. (3). Therefore,

$$\delta\mathcal{E}(\mathbf{p})=2|V_{11}(\mathbf{p})|, \tag{C3}$$

and, barring a special case, equation $\delta\mathcal{E}(\mathbf{p})=0$ defines a $(d-1)$-dimensional surface of zero $g_\perp(\mathbf{p})$ in d-dimensional momentum space. The Kramers degeneracy subset contains, at the very least, the star of the momentum $\mathbf{p}=\mathbf{Q}/2$ [see Eq. (6) and the subsequent discussion] and the $(\mathbf{k}\cdot\mathbf{p})$ expansion[91] around these points shows that they are not isolated, but rather belong to a $(d-1)$-dimensional manifold. The latter is continuous, with the obvious exception of $d=1$.

Finally, notice that, according to Eq. (C3), $\delta\mathcal{E}(\mathbf{p})$ is periodic with the antiferromagnetic ordering wave vector $\mathbf{Q}$,

$$\delta\mathcal{E}(\mathbf{p}+\mathbf{Q})=\delta\mathcal{E}(\mathbf{p}), \tag{C4}$$

thanks to $\mathbf{Q}$ being a reciprocal-lattice vector in the antiferromagnetic state. Therefore, properties (16) and (17) are indeed model-independent, as opposed to hinging on an approximation of the weak-coupling model (8).

APPENDIX D: REVISITING REF. 14

In Ref. 14, Brazovskii and Lukyanchuk stated that operator $\mathbf{\Lambda}=(\mathbf{n}\cdot\boldsymbol{\sigma})$ exchanges the momenta $\mathbf{p}$ and $\mathbf{p}+\mathbf{Q}$ in Eq. (8) and thus represents the momentum boost by the ordering

wave vector $\mathbf{Q}$ in reciprocal space. In a commensurate antiferromagnetic state, $\mathbf{Q}$ becomes a reciprocal-lattice vector and thus $\mathbf{\Lambda}$ must be a symmetry of the Hamiltonian. With the assumption of the effective Zeeman coupling (1), this lead the authors of Ref. 14 to the relation $g_\perp(\mathbf{p}+\mathbf{Q})=-g_\perp(\mathbf{p})$ [Eq. (16) of the present work], and to the conclusion that $g_\perp(\mathbf{p})=0$ at the MBZ boundary. Unfortunately, while this beautiful result is indeed correct for a lattice of square symmetry, several circumstances prevent one from embracing these arguments.

Most importantly, they hinge solely on the symmetry under translation by $\mathbf{Q}$, put otherwise—on commensurability of magnetic order with the crystal lattice. If correct, this would imply that, in an arbitrary commensurate Néel antiferromagnet, Kramers degeneracy takes place at the entire MBZ boundary regardless of the underlying crystal symmetry. The toy example (18) with $\eta \neq 1$ shows that this is not at all necessarily the case.

Indeed, for a generic crystal symmetry, the condition $g_\perp(\mathbf{p}+\mathbf{Q})=-g_\perp(\mathbf{p})$ [see Ref. 14 and Eq. (16)] does *not*, by itself, restrict the manifold $g_\perp(\mathbf{p})=0$ to the MBZ boundary. However, the Kramers subset of the manifold of degenerate states can be obtained by combining Eq. (16) with the crystal symmetries (see Sec. III A). For instance, combined with the inversion symmetry $g_\perp(-\mathbf{p})=g_\perp(\mathbf{p})$, Eq. (16) stipulates that $g_\perp(\mathbf{Q}/2)=0$. Similarly, disappearance of $g_\perp(\mathbf{p})$ at the entire MBZ boundary for the square-symmetry case can be obtained by using Eq. (16) and the point symmetries of the square lattice. For a finite as opposed to infinitesimal field, these results were established in Sec. II and in the first two examples in Sec. IV.

On a more technical level, the operator $\mathbf{\Lambda}$ is equivalent to $\mathbf{U_n}(\pi)$ and thus inverts the sign of the transverse component of the field. Hence, in a field with nonzero transverse component $\mathbf{H}_\perp$, $\mathbf{\Lambda}$ ceases to be a symmetry of the Hamiltonian, in agreement with the first line of Table I—and thus can no longer represent the momentum boost by $\mathbf{Q}$.

*Present address: Department of Physics and Astronomy, University of South Carolina, Columbia, SC 29208, USA.

[1] E. Fawcett, Rev. Mod. Phys. **60**, 209 (1988).
[2] E. Fawcett, H. L. Alberts, V. Yu. Galkin, D. R. Noakes, and J. V. Yakhmi, Rev. Mod. Phys. **66**, 25 (1994).
[3] N. I. Kulikov and V. V. Tugushev, Usp. Fiz. Nauk **144**, 643 (1984) [Sov. Phys. Usp. **27**, 954 (1984)].
[4] K.-H. Müller and V. N. Narozhnyi, Rep. Prog. Phys. **64**, 943 (2001).
[5] R. J. Birgeneau, C. Stock, J. M. Tranquada, and K. Yamada, J. Phys. Soc. Jpn. **75**, 111003 (2006).
[6] John M. Tranquada, in *Handbook of High-Temperature Superconductivity*, edited by J. Robert Schrieffer and James S. Brooks (Springer, New York, 2007).
[7] C. de la Cruz, Q. Huang, J. W Lynn, J. Li, W. Ratcliff II, J. L. Zarestky, H. A. Mook, G. F. Chen, J. L. Luo, N. L. Wang, and P. Dai, Nature (London) **453**, 899 (2008).
[8] P. M. Chaikin, J. Phys. I **6**, 1875 (1996).
[9] Y. Kuramoto and Y. Kitaoka, *Dynamics of Heavy Electrons* (Clarendon, Oxford, 2000).
[10] R. A. Robinson, in *Magnetism in Heavy Fermion Systems*, edited by H. B. Radousky (World Scientific, Singapore, 2000).
[11] J. Flouquet, in *Progress in Low Temperature Physics*, edited by W. P. Halperin (Elsevier B.V., 2005), Vol. XV, Chap. 2.
[12] C. Herring, in *Magnetism*, edited by G. T. Rado and H. Suhl (Academic Press Inc., New York and London, 1966), Vol. IV, Chap. XIII.
[13] J. O. Dimmock and R. G. Wheeler, Phys. Rev. **127**, 391 (1962).
[14] S. A. Brazovskii and I. A. Luk'yanchuk, Zh. Eksp. Teor. Fiz. **96**, 2088 (1989) [Sov. Phys. JETP **69**, 1180 (1989)].
[15] S. A. Brazovskii, I. A. Luk'yanchuk, and R. R. Ramazashvili, Pis'ma Zh. Eksp. Teor. Fiz. **49**, 557 (1989) [JETP Lett. **49**, 644 (1989)].
[16] R. Ramazashvili, Phys. Rev. Lett. **101**, 137202 (2008).
[17] A. F. Andreev and V. I. Marchenko, Usp. Fiz. Nauk **130**, 39 (1980) [Sov. Phys. Usp. **23**, 21 (1980)].
[18] H. Zabel, J. Phys.: Condens. Matter **11**, 9303 (1999).
[19] J. M. Lawrence and S. M. Shapiro, Phys. Rev. B **22**, 4379 (1980).
[20] G. Knebel, D. Braithwaite, P. C. Canfield, G. Lapertot, and J. Flouquet, Phys. Rev. B **65**, 024425 (2001).
[21] T. Ebihara, N. Harrison, M. Jaime, S. Uji, and J. C. Lashley, Phys. Rev. Lett. **93**, 246401 (2004).
[22] F. M. Grosche, I. R. Walker, S. R. Julian, N. D. Mathur, D. M. Freye, M. J. Steiner, and G. G. Lonzarich, J. Phys.: Condens. Matter **13**, 2845 (2001).
[23] P. Dervenagas, D. Kaczorowski, F. Bourdarot, P. Burlet, A. Czopnik, and G. H. Lander, Physica B **269**, 368 (1999).
[24] M. H. van Maaren, H. J. van Daal, K. H. J. Buschow, and C. J. Schinkel, Solid State Commun. **14**, 145 (1974).
[25] A. L. Cornelius, A. J. Arko, J. L. Sarrao, J. D. Thompson, M. F. Hundley, C. H. Booth, N. Harrison, and P. M. Oppeneer, Phys. Rev. B **59**, 14473 (1999).
[26] D. Aoki, N. Suzuki, K. Miyake, Y. Inada, R. Settai, K. Sugiyama, E. Yamamoto, Y. Haga, Y. Ōnuki, T. Inoue, K. Kindo, H. Sugawara, H. Sato, and H. Yamagami, J. Phys. Soc. Jpn. **70**, 538 (2001).
[27] A. Murasik, J. Leciejewicz, S. Ligenza, and A. Misiuk, Phys. Status Solidi A **20**, 395 (1973).
[28] Y. Tokiwa, D. Aoki, Y. Haga, E. Yamamoto, S. Ikeda, R. Settai, A. Nakamura, and Y. Ōnuki, J. Phys. Soc. Jpn. **70**, 3326 (2001).
[29] J. Lawrence, Phys. Rev. B **20**, 3770 (1979).
[30] S. Nasu, A. M. van Diepen, H. H. Neumann, and R. S. Craig, J. Phys. Chem. Solids **32**, 2773 (1971).
[31] I. R. Walker, F. M. Grosche, D. M. Freye, and G. G. Lonzarich, Physica C **282-287**, 303 (1997).
[32] N. D. Mathur, F. M. Grosche, S. R. Julian, I. R. Walker, D. M. Freye, R. K. W. Haselwimmer, and G. G. Lonzarich, Nature (London) **394**, 39 (1998).
[33] M. Endo, N. Kimura, H. Aoki, T. Terashima, S. Uji, T. Matsumoto, and T. Ebihara, Phys. Rev. Lett. **93**, 247003 (2004).
[34] M. Biasini, G. Ferro, and A. Czopnik, Phys. Rev. B **68**, 094513

(2003).
[35] L. P. Gor'kov and P. D. Grigoriev, Phys. Rev. B **73**, 060401(R) (2006).
[36] T. Ebihara, I. Umehara, A. K. Albessard, K. Satoh, and Y. Ōnuki, J. Phys. Soc. Jpn. **61**, 1473 (1992).
[37] J. Rusz and M. Biasini, Phys. Rev. B **71**, 233103 (2005).
[38] N. A. Curry, Proc. Phys. Soc. London **86**, 1193 (1965).
[39] M. Nakashima, Y. Haga, E. Yamamoto, Y. Tokiwa, M. Hedo, Y. Uwatoko, R. Settai, and Y. Ōnuki, J. Phys.: Condens. Matter **15**, S2007 (2003).
[40] F. Steglich, J. Aarts, C. D. Bredl, W. Lieke, D. Meschede, W. Franz, and H. Schäfer, Phys. Rev. Lett. **43**, 1892 (1979).
[41] G. Knopp, A. Loidl, K. Knorr, L. Pawlak, M. Duczmal, R. Caspary, U. Gottwick, H. Spille, F. Steglich, and A. P. Murani, Z. Phys. B: Condens. Matter **77**, 95 (1989).
[42] D. Jaccard, K. Behnia, and J. Sierro, Phys. Lett. A **163**, 475 (1992).
[43] F. M. Grosche, S. R. Julian, N. D. Mathur, G. G. Lonzarich, Physica B **223**, 50 (1996).
[44] I. Sheikin, A. Gröger, S. Raymond, D. Jaccard, D. Aoki, H. Harima, and J. Flouquet, Phys. Rev. B **67**, 094420 (2003).
[45] B. H. Grier, J. M. Lawrence, V. Murgai, and R. D. Parks, Phys. Rev. B **29**, 2664 (1984).
[46] S. Kawarazaki, M. Sato, Y. Miyako, N. Chigusa, K. Watanabe, N. Metoki, Y. Koike, and M. Nishi, Phys. Rev. B **61**, 4167 (2000).
[47] M. Ohashi, G. Oomi, S. Koiwai, M. Hedo, and Y. Uwatoko, Phys. Rev. B **68**, 144428 (2003).
[48] R. Movshovich, T. Graf, D. Mandrus, J. D. Thompson, J. L. Smith, and Z. Fisk, Phys. Rev. B **53**, 8241 (1996).
[49] S. Araki, R. Settai, T. C. Kobayashi, H. Harima, and Y. Ōnuki, Phys. Rev. B **64**, 224417 (2001).
[50] P. Burlet, J. M. Effantin, J. Rossat-Mignod, S. Kunii, and T. Kasuya, J. Phys. (Paris), Colloq. C8, Suppl. 12, **49**, 459 (1988).
[51] R. M. Galera, D. P. Osterman, J. D. Axe, S. Kunii, and T. Kasuya, J. Appl. Phys. **63**, 3580 (1988).
[52] D. F. McMorrow, K. A. McEwen, J.-G. Park, S. Lee, D. Mannix, F. Iga, and T. Takabatake, Physica B **345**, 66 (2004).
[53] C. M. McCarthy and C. W. Tompson, J. Phys. Chem. Solids **41**, 1319 (1980).
[54] Y. Onuki, A. Umezawa, W. K. Kwok, G. W. Crabtree, M. Nishihara, T. Yamazaki, T. Omi, and T. Komatsubara, Phys. Rev. B **40**, 11195 (1989).
[55] R. G. Goodrich, N. Harrison, and Z. Fisk, Phys. Rev. Lett. **97**, 146404 (2006).
[56] Y. Kubo, S. Asano, H. Harima, and A. Yanase, J. Phys. Soc. Jpn. **62**, 205 (1993).
[57] J. Stankiewicz, S. Nakatsuji, and Z. Fisk, Phys. Rev. B **71**, 134426 (2005).
[58] E. M. Motoyama, G. Yu, I. M. Vishik, O. P. Vajk, P. K. Mang, and M. Greven, Nature (London) **445**, 186 (2007).
[59] M. Matsuda, Y. Endoh, K. Yamada, H. Kojima, I. Tanaka, R. J. Birgeneau, M. A. Kastner, and G. Shirane, Phys. Rev. B **45**, 12548 (1992).
[60] N. P. Armitage, F. Ronning, D. H. Lu, C. Kim, A. Damascelli, K. M. Shen, D. L. Feng, H. Eisaki, Z.-X. Shen, P. K. Mang, N. Kaneko, M. Greven, Y. Onose, Y. Taguchi, and Y. Tokura, Phys. Rev. Lett. **88**, 257001 (2002).
[61] Nicolas Doiron-Leyraud, Cyril Proust, David LeBoeuf, Julien Levallois, Jean-Baptiste Bonnemaison, Ruixing Liang, D. A. Bonn, W. N. Hardy, and Louis Taillefer, Nature (London) **447**, 565 (2007).
[62] R. J. Cava, in *Rare Earth Transition Metal Borocarbides (Nitrides): Superconducting, Magnetic and Normal State Properties*, edited by K.-H. Müller and V. N. Narozhnyi (Kluwer, Dordrecht, 2001), p. 21.
[63] Y. Iwasa, K. Mizuhashi, T. Koda, Y. Tokura, and G. Saito, Phys. Rev. B **49**, 3580 (1994).
[64] H. Uozaki, T. Sasaki, S. Endo, and N. Toyota, J. Phys. Soc. Jpn. **69**, 2759 (2000).
[65] C. Coulon and R. Clérac, Chem. Rev. (Washington, D.C.) **104**, 5655 (2004).
[66] K. Miyagawa, A. Kawamoto, Y. Nakazawa, and K. Kanoda, Phys. Rev. Lett. **75**, 1174 (1995).
[67] P. Wzietek, S. Lefebvre, H. Mayaffre, S. Brown, C. Bourbonnais, D. Jérome, C. Mézière, and P. Batail, Hyperfine Interact. **128**, 183 (2000).
[68] P. Foury-Leylekian, D. Le Bolloc'h, B. Hennion, S. Ravy, A. Moradpour, and J.-P. Pouget, Phys. Rev. B **70**, 180405(R) (2004).
[69] J.-P. Pouget, P. Foury-Leylekian, D. Le Bolloc'h, B. Hennion, S. Ravy, C. Coulon, V. Cardoso, and A. Moradpour, J. Low Temp. Phys. **142**, 147 (2006).
[70] P. Foury-Leylekian, S. Petit, C. Coulon, B. Hennion, A. Moradpour, and J.-P. Pouget, Physica B **404**, 537 (2009).
[71] S. Lefebvre, P. Wzietek, S. Brown, C. Bourbonnais, D. Jérome, and C. Mézière, Physica B **312**, 578 (2002).
[72] F. Kagawa, K. Miyagawa, and K. Kanoda, Nature (London) **436**, 534 (2005).
[73] K. Kanoda, Physica C **282-287**, 299 (1997); private communication (2008).
[74] N. Biškup, L. Balicas, S. Tomić, D. Jérome, and J.-M. Fabre, Phys. Rev. B **50**, 12721 (1994).
[75] X. Xiao, T. Hayashi, H. Fujiwara, T. Sugimoto, S. Noguchi, Y. Weng, H. Yoshino, K. Murata, and H. A. Katori, J. Am. Chem. Soc. **129**, 12618 (2007).
[76] W. Suzuki, E. Fujiwara, A. Kobayashi, Y. Fujishiro, E. Nishibori, M. Takata, M. Sakata, H. Fujiwara, and H. Kobayashi, J. Am. Chem. Soc. **125**, 1486 (2003).
[77] B. Zhou, M. Shimamura, E. Fujiwara, A. Kobayashi, T. Higashi, E. Nishibori, M. Sakata, HengBo Cui, Kazuyuki Takahashi, and Hayao Kobayashi, J. Am. Chem. Soc. **128**, 3872 (2006).
[78] Y. Hara, K. Miyagawa, K. Kanoda, M. Shimamura, B. Zhou, A. Kobayashi, and H. Kobayashi, J. Phys. Soc. Jpn. **77**, 053706 (2008).
[79] J. M. Barandiaran, D. Gignoux, D. Schmitt, J. C. Gomez-Sal, J. Rodriguez Fernandez, P. Chieux, and J. Schweizer, J. Magn. Magn. Mater. **73**, 233 (1988).
[80] E. Granado, B. Uchoa, A. Malachias, R. Lora-Serrano, P. G. Pagliuso, and H. Westfahl, Jr., Phys. Rev. B **74**, 214428 (2006).
[81] M. Rotter, M. Loewenhaupt, M. Doerr, A. Lindbaum, H. Sassik, K. Ziebeck, and B. Beuneu, Phys. Rev. B **68**, 144418 (2003).
[82] P. M. Grant, Nature (London) **453**, 1000 (2008).
[83] H. Takahashi, K. Igawa, K. Arii, Y. Kamihara, M. Hirano, and H. Hosono, Nature (London) **453**, 376 (2008).
[84] Y. Kamihara, H. Hiramatsu, M. Hirano, R. Kawamura, H. Yanagi, T. Kamiya, and H. Hosono, J. Am. Chem. Soc. **128**, 10012 (2006).
[85] E. P. Wigner, *Group Theory and its Application to the Quantum Mechanics of Atomic Spectra* (Academic, New York, 1971).

[86] C. Herring, Phys. Rev. **52**, 361 (1937).
[87] A. Shengelaya, H. Keller, K. A. Müller, B. I. Kochelaev, and K. Conder, Phys. Rev. B **63**, 144513 (2001).
[88] R. R. Ramazashvili, Zh. Eksp. Teor. Fiz. **100**, 915 (1991) [Sov. Phys. JETP **73**, 505 (1991)].
[89] R. Ramazashvili, arXiv:0808.3946 (unpublsihed).
[90] V. V. Kabanov and A. S. Alexandrov, Phys. Rev. B **77**, 132403 (2008).
[91] C. Kittel, *Quantum Theory of Solids* (Wiley, New York, 1987).